DESIGN OF QUASI-SATELLITE SCIENCE ORBITS AT DEIMOS

A Thesis

Submitted to the Faculty

of

Purdue University

by

Michael R. Thompson

In Partial Fulfillment of the

Requirements for the Degree

of

Master of Science in Aeronautics and Astronautics

December 2020

Purdue University

West Lafayette, Indiana

THE PURDUE UNIVERSITY GRADUATE SCHOOL
STATEMENT OF THESIS APPROVAL

Dr. David A. Spencer, Chair

School of Aeronautics and Astronautics, NASA Jet Propulsion Laboratory

Dr. Kathleen Howell

School of Aeronautics and Astronautics

Dr. Carolin Frueh

School of Aeronautics and Astronautics

Approved by:

Dr. Gregory Blaisdell

Professor and Associate Head of Gambaro Graduate Program of Aeronautics and Astronautics

To R.H., who sent me down this path nearly two decades ago.

ACKNOWLEDGMENTS

"If I have seen further it is by standing on the shoulders of Giants."

First and foremost, I would like to acknowledge every author cited in this thesis, and the additional ones that have informed this work. The literature that has either directly or indirectly influenced this work is the foundation upon which any additional contributions here are built.

I would also like to thank my three committee members individually.

Professor Frueh, who taught the first dynamics class I ever took during my undergraduate education in 2015 and later introduced me to many of the SSA topics I now use in my professional and personal studies.

Professor Howell, who gave me my first glimpse at astrodynamics and multi-body dynamics, a topic that has guided me ever since.

And my advisor Professor Spencer, who guided my research and provided insight into the way that actual space flight missions are designed and operated. JPL is lucky to have him back and leading the charge for Mars Sample Return.

My former lab mate Mitch Dominguez wrote the bulk of the low-level coverage algorithm which has been very useful in performing sensor trades and science orbit analyses. Outside of the specific contributions of Mitch, the entire SFPL research group has been very helpful during my time here, and I can't wait to see everything the group goes off to accomplish over the coming years.

I will always be thankful for the entire team at Advanced Space in Boulder, CO, who brought me in and threw me into the fire on a number of truly difficult and exciting programs. I'm looking forward to being able to dedicate all of my time towards this team post-graduation.

Finally, I would like to give thanks to Ashley and our two cats Squid and Otis for supporting me throughout graduate school. The support of all three has without

a doubt made my time in graduate school much more manageable, and I'm looking forward to post-grad school life with them.

TABLE OF CONTENTS

Page

LIST OF TABLES viii

LIST OF FIGURES ix

ABBREVIATIONS xii

ABSTRACT xiii

1 INTRODUCTION 1
1.1 Previous and Future Missions to Martian Moons 2
1.1.1 Previous Missions 2
1.1.2 Current Missions 3
1.1.3 Future Missions en Route or in Development 4
1.1.4 Future Mission Concept Studies 5
1.2 Thesis Introduction and Organization 6
1.2.1 Previous Studies of the Deimos System Dynamics 6
1.2.2 Improvements Upon the State of the Art 9
1.2.3 Thesis Organization 9

2 MATHEMATICAL FRAMEWORKS 11
2.1 Circular Restricted Three-Body Problem 11
2.2 Targeting Periodic Orbits via the State Transition Matrix 15
2.2.1 Finite Differencing 16
2.2.2 STM Integration 16
2.2.3 STM-Based Targeting for Periodic Orbits 17
2.3 Periodic Orbit Stability Index 19
2.4 Numerical Targeting in GMAT 20
2.5 Ephemeris Model Dynamics and Planetary Constants 21

3 PERIODIC AND QUASI-PERIODIC ORBITS AT DEIMOS 25
3.1 Mars - Deimos Rotating Frame Definition 26
3.2 Lagrange Points at Deimos 27
3.3 Prograde Orbits About Deimos 28
3.4 Distant Retrograde Orbits 29
3.5 Quasi-Satellite Orbits 36

4 MISSION ANALYSIS AT DEIMOS 41
4.1 Stability of Quasi-Satellite Orbits at Deimos 41
4.1.1 Theoretical Approach 42

Page

4.1.2 Numerical Approach 43
4.2 Science Orbit Design 47
4.2.1 Batch Search 47
4.2.2 Long-Term Coverage Analysis of Selected QSOs 61
4.3 Deimos Lighting Conditions 71
4.4 Deimos DRO Sensitivity 73
4.5 Transfers Between Orbits 77
4.5.1 Along-Track Three-Burn Strategy 77
4.5.2 Radial Three-Burn Strategy 77

5 CONCLUSIONS AND FUTURE WORK 82
5.1 Recommendations for Future Work 83

REFERENCES 86

VITA 91

LIST OF TABLES

Table Page

2.1 Spacecraft Force Model and Dynamic Setup 24

4.1 Deimos Coverage Cases Evaluated 47

4.2 Deimos Long-Term Coverage Cases Evaluated 61

4.3 Long-Term Coverage Analysis 65

LIST OF FIGURES

Figure Page

1.1 All operational Mars orbiters as of December 2020. 3

2.1 The general three-body problem. 12

2.2 The three-body problem redrawn with CRTBP assumptions. 13

2.3 A method for targeting periodic orbits in the CRTBP. 18

2.4 Accelerations due to Mars and Deimos as a function of distance from Deimos. 23

3.1 The Deimos shape model developed by Thomas (2000) [45]. Visualized in the Small Body Mapping Tool [46]. 25

3.2 The Deimos-centered Mars - Deimos rotating frame. Not to scale. 26

3.3 The Mars - Deimos L1 and L2 Lagrange points with respect to the shape model in the Mars - Deimos rotating frame. 27

3.4 The g family of orbits about Deimos in the Mars - Deimos rotating frame. 29

3.5 The g' family of orbits about Deimos in the Mars - Deimos rotating frame. 30

3.6 The f family of orbits about Deimos in the Mars - Deimos rotating frame. 31

3.7 Ratio of the Y amplitude to X amplitude as the f family grows. 32

3.8 Period of the f family of orbits about Deimos compared to the Deimos period about Mars. 32

3.9 Initial conditions for the f family of orbits about Deimos. 34

3.10 Stability index of the f family of orbits about Deimos. 34

3.11 Example member of the f family as viewed in the Deimos-centered inertial frame from above. 35

3.12 Example member of the f family as viewed in the Deimos-centered inertial frame. Mars included for spatial awareness. 36

3.13 Example QSO as viewed in the Mars - Deimos rotating frame. 38

3.14 QSO as viewed in the Deimos-centered inertial frame from above. 39

3.15 QSO as viewed in the Deimos-centered inertial frame from the Mars - Deimos orbital plane. 40

Figure Page

4.1 Stability map of Deimos QSOs based on CRTBP dynamics. Blue: Remains in orbit about Deimos. Red: Impacts or leaves the vicinity of Deimos. 44

4.2 Critical inclination across the f family. 45

4.3 Percent coverage for thermal infrared measurements at 5 m/px using the FLIR Tau 2 60mm lens. 50

4.4 Percent coverage for thermal infrared measurements at 5 m/px using the FLIR Tau 2 100mm lens. 51

4.5 Percent coverage for thermal infrared measurements at 10 m/px using the FLIR Tau 2 60mm lens. 52

4.6 Percent coverage for thermal infrared measurements at 10 m/px using the FLIR Tau 2 100mm lens. 53

4.7 Percent coverage for thermal infrared measurements at 30 m/px using the FLIR Tau 2 60mm lens. 55

4.8 Percent coverage for thermal infrared measurements at 30 m/px using the FLIR Tau 2 100mm lens. 56

4.9 Percent coverage for visual measurements at 5 m/px using the ECAM C30 30mm lens. 57

4.10 Percent coverage for visual measurements at 5 m/px using the ECAM C50 12.6mm lens. 58

4.11 Percent coverage for visual measurements at 5 m/px using the ECAM C50 30mm lens. 59

4.12 Percent coverage for visual measurements at 5 m/px using the ECAM C50 63mm lens. 60

4.13 Solar incidence and elevation angle conventions. 62

4.14 Mapping between QSO initial conditions and inclination with respect to Deimos. 64

4.15 Maneuver strategy for maintaining long-term QSOs. 65

4.16 Selected QSO that maximizes coverage for analyzed cases. 70

4.17 Surface coverage of Deimos for the Thermal Infrared Sunlit case. 71

4.18 Solar latitude at Deimos over a period of 5 years. 72

4.19 $\dot{Y}_0$ sensitivities. Blue: Remains in orbit about Deimos. Red: Impacts or leaves the vicinity of Deimos. 74

Figure Page

4.20 $\dot{X}_0$ sensitivities. Blue: Remains in orbit about Deimos. Red: Impacts or leaves the vicinity of Deimos. 75

4.21 $\dot{X}_0$ sensitivities. Blue: Remains in orbit about Deimos. Red: Impacts or leaves the vicinity of Deimos. 76

4.22 Three-burn along-track strategy for transfers at Deimos. 78

4.23 A map of transfers between members of the f family via the Along-Track Three-Burn Strategy in m/s. 79

4.24 Three-burn radial strategy for transfers at Deimos. 80

4.25 A map of transfers between members of the f family via the Radial Three-Burn Strategy in m/s. 81

ABBREVIATIONS

AFIT	Air Force Institute of Technology
CONOPS	concept of operations
CRISM	Compact Reconnaissance Imaging Spectrometer for Mars
CRTBP	circular restricted three-body problem
DRO	distant retrograde orbit
ESA	European Space Agency
GMAT	General Mission Analysis Tool
HiRISE	High Resolution Imaging Science Experiment
IAU	International Astronautical Union
ISRU	in-situ resource utilization
JAXA	Japan Aerospace Exploration Agency
MAVEN	Mars Atmosphere and Volatile Evolution
MERLIN	Mars-Moon Exploration Reconnaissance and Landed Investigation
MMX	Mars Moon Exploration
MRO	Mars Reconnaissance Orbiter
NASA	National Aeronautics and Space Administration
PSDS3	Planetary Science Deep Space SmallSat Studies Program
QSO	quasi-satellite orbit
SIMPLEx	Small Innovative Missions for Planetary Exploration
STM	state transition matrix

ABSTRACT

Thompson, Michael R. M.S., Purdue University, December 2020. Design of Quasi-Satellite Science Orbits at Deimos. Major Professor: David A. Spencer.

In order to answer the most pressing scientific questions about the two Martian moons, Phobos and Deimos, new remote sensing observations are required. The best way to obtain global high resolution observations of Phobos and Deimos is through dedicated missions to each body that utilize close-proximity orbits, however much of the orbital tradespace is too unstable to realistically or safely operate a mission.

This thesis explores the dynamics and stability characteristics of trajectories near Deimos. The family of distant retrograde orbits that are inclined out of the Deimos equatorial plane, known as quasi-satellite orbits, are explored extensively. To inform future mission design and CONOPS, the sensitivities and stability of distant retrograde and quasi-satellite orbits are examined in the vicinity of Deimos, and strategies for transferring between DROs are demonstrated. Finally, a method for designing quasi-satellite science orbits is demonstrated for a set of notional instruments and science requirements for a Deimos remote sensing mission.

1. INTRODUCTION

The exploration of Phobos and Deimos, the two small moons of Mars, is attractive from both a planetary science and human exploration standpoint. In planetary science, the origins of both objects remain a mystery. From the limited data on the bodies, they both appear to have similar properties as D-type asteroids that are very common in the outer asteroid belt and in the Jovian system (low density, low albedo, red spectrum in both the visible and near-infrared wavelengths), but the nearly-circular stable orbits of Phobos and Deimos generally do not support a hypothesis involving asteroid capture [1–4].

If asteroid capture is not a viable model, another set of models have hypothesized Phobos and Deimos forming in the Martian system, either at the same time as Mars, from debris of a large Martian impact, or in a cyclical breakup and formation over time [1, 2]. But the limited spectral data that does exist for the two moons does not resemble known Martian materials [1, 5].

These two major theories for the origins of Phobos and Deimos obviously both contain unanswered questions that likely cannot be resolved without new, global, and high resolution observations of each body. Ground-based optical and radar observations of both moons are possible, but these observations only yield high-level properties of the moons and do not allow for resolving how the composition and properties change at different points on the surface [6]. A dedicated mission to one or both of these moons is the best way to obtain high resolution, global observations in the near-term.

In addition to these planetary science-focused motivations, there is a second set of motivations relating to human spaceflight. Both Martian moons have long been viewed as possible staging points for future human exploration [2, 7]. This staging could come in the form of in-situ resource utilization (ISRU) through the use of raw

materials, as a base for control of surface operations, or a final staging point prior to entry, descent, and landing. However, without additional observations of either body, the feasibility of ISRU and challenges of operating in the Phobos or Deimos vicinity are ultimately unknown.

1.1 Previous and Future Missions to Martian Moons

1.1.1 Previous Missions

To date, there have been no fully successful missions dedicated to studying Phobos or Deimos. The Soviet Union launched *Phobos 1* and *Phobos 2* in 1988, but both suffered failures, the former within 2 months of launch, and the latter 57 days after Mars orbit insertion, but prior to the start of the primary science phase of the mission [8]. After Mars orbit insertion, *Phobos 2* did successfully maneuver into a relative orbit with Phobos with a closest approach of 200 km, but suffered an electronics failure before the more novel phase of the mission, which involved an approach as close as 50 m, the deployment of two small landers, and probing experiments of the Phobos surface [8]. *Phobos 2* provided some scientific data on the moon, including imagery, spectral, and other remote sensing data, but ultimately fell short of its original scientific goals [9]. The Russian *Phobos-Grunt* mission was launched in 2011, with the goal of collecting and returning samples from the Phobos surface, but suffered an early operations failure in its initial parking orbit and re-entered Earth's atmosphere less than two months later [2, 10].

Other non-dedicated previous missions that have provided data on Phobos and Deimos either during Martian flybys or as part of a more Mars-focused mission include *Mariner 4, 5, 6, 7* and *9*, *Rosetta*, *Viking 1* and *2*, *Mars Global Surveyor*, *Mars Pathfinder*, and the *Mars Exploration Rovers Spirit and Opportunity* [11]. For lander missions, observations of Phobos or Deimos have typically been limited to a few images from the Martian surface. These non-dedicated missions have provided valuable data well beyond what is possible with ground-based observations, but the

data is still insufficient for answering some of the big questions about the origins of each moon and whether they might provide opportunities for ISRU in the future.

1.1.2 Current Missions

Many of the missions currently operating at Mars can provide occasional observations of Phobos and Deimos, but again, there are no missions dedicated to the study of the bodies.

Out of all currently operating Mars orbiters, *MAVEN*, *Mars Express*, and *Mangalyaan (Mars Orbiter Mission)* occasionally provide close-approaches of Phobos, but there are none that provide close approaches of Deimos, leaving the amount of data on the body relatively sparse. The *Mars Reconnaissance Orbiter* (*MRO*) provides no close-approaches of Phobos or Deimos, but its High Resolution Imaging Science Experiment (HiRISE) and hyper-spectral Compact Reconnaissance Imaging Spectrometer for Mars (CRISM) have both provided a number of observations of Phobos and Deimos, and will continue to do so for the foreseeable future [11].

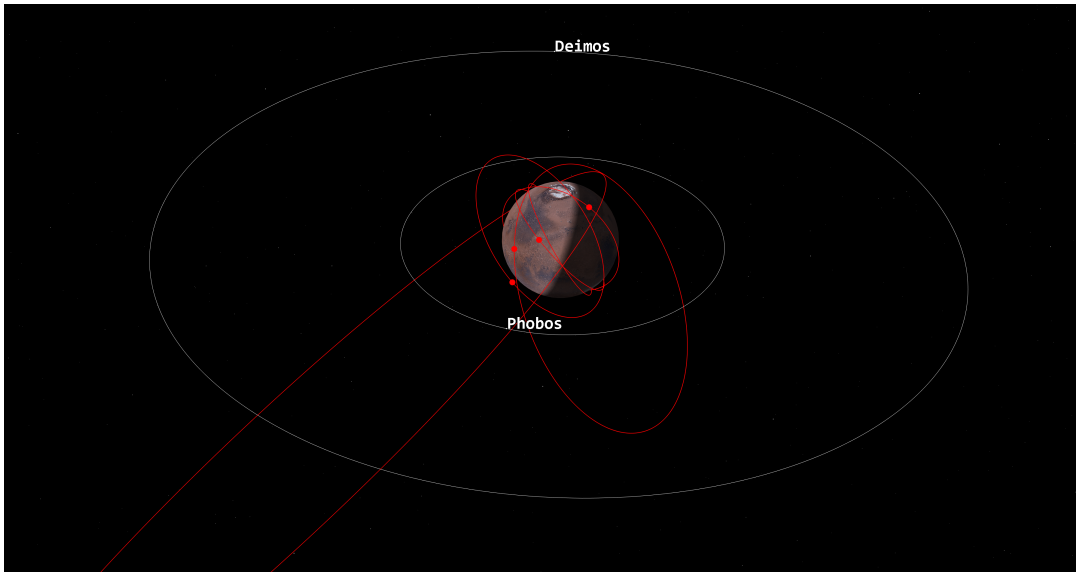

Figure 1.1. All operational Mars orbiters as of December 2020.

The *Mars Express* mission has been particularly useful in obtaining observations of Phobos due to its eccentric orbit. The mission has provided flybys as close as 77 km from Phobos, which has allowed for updates to the Phobos ephemeris, shape models, mass properties, composition models, and other properties [12]. However, the apoapsis of the *Mars Express* mission is nowhere near the orbital distance of Deimos, and the closest observations of the smaller Martian moon have been from around 10,000 km away [12]. This distance is much too great for the high-resolution observations of Deimos that are desired by those who wish to understand its origins.

1.1.3 Future Missions en Route or in Development

Future Mars missions that utilize an orbiter are likely to provide some amount of occasional data on Phobos and Deimos in the same way that many current missions do. The periapsis of the science orbit for the *Hope* orbiter of the Emirates Mars Mission is very close to that of Deimos, which could provide an opportunity for close approaches, but this is not currently planned in the reference mission [13].

The mission under development that has the greatest potential to expand our understanding of Martian moons is the Japanese *Mars Moon Exploration (MMX)*, currently set to launch in 2024. This mission will rendezvous with Phobos, collect up to 10 kg of surface samples, and return to Earth [14]. If successful, the mission will provide by far the most detailed look at Phobos achieved by any mission. The mission also has an option to introduce Deimos flybys at minimal fuel cost, and this is a concept that is being considered as the mission is developed [14].

Sample return provides revolutionary advantages for studying the Martian system over remote sensing observations [2]. Out of missions currently en route to Mars or in the late stages of development, *MMX* provides the best opportunity to expand our knowledge on the questions of the origins of Martian moons and the potential for ISRU.

1.1.4 Future Mission Concept Studies

Chariot is a NASA Small Innovative Missions for Planetary Exploration (SIMPLEx)-class mission concept to send a small spacecraft to explore Phobos and Deimos. The mission concept was developed in 2017 under the Planetary Science Deep Space SmallSat Studies Program (PSDS3) at Purdue University [1].

This study developed the mission architecture and basic systems engineering for a CubeSat mission to Phobos and Deimos that would perform visual, near-infrared, and thermal-infrared observations of each body [1].

The mission would utilize a 12U CubeSat platform which provides some key constraints on the mission when compared to a larger Discovery or New Frontiers-class mission [1]. For example, with this small satellite platform, finding stable science orbits is critical - frequent stationkeeping maneuvers may be operationally infeasible. Additionally, to perform high-resolution science observations of each Moon, a small satellite platform must utilize a close-proximity trajectory. More capable spacecraft can carry large sensors that can make high-resolution observations from a large stand-off distance, but this is physically not possible for a small spacecraft.

Another mission in development focused on the Martian moons is the ESA *DePhine* (Deimos and Phobos Interior Explorer) Mission [15]. This is an ESA M-class mission, which has a cost cap of approximately 500 million Euros, analogous to a NASA Discovery-class mission.

The *DePhine* mission baselines a very close relative orbit with Deimos (8 - 12 km above the surface) and provides CONOPS for flybys as low as 1 - 2 km [15]. After a 10 month Deimos phase is complete, *DePhine* will transition into a 2:1 resonant orbit with Phobos and perform flybys at altitudes as low as 50 km [15]. The spacecraft will be outfitted with a suite of remote sensing instruments, a subsurface radar, and a gravity science package, which will allow for detailed study of the composition and interior of each body [15].

1.2 Thesis Introduction and Organization

The original mission concepts for both *Chariot* and *DePhine* studied concepts for visiting both Phobos and Deimos in one mission [1,15]. As such, studying the orbital dynamics and mission operations about both bodies is a rich area of potential study to facilitate future scientific discovery. This thesis will focus on proximity operations and science orbit design about Deimos.

Mission design and operations at Deimos are emphasized over Phobos for a number of reasons. Given that multiple missions have attempted to study Phobos, and there are more currently in development, the dynamic environment about Phobos is well-studied when compared to that of Deimos [10, 16–18]. The understanding of the environment about Phobos is only continuing to advance in recent years given the current progress of the *MMX* mission design teams [19, 20]. A better understanding of the dynamic environment about Deimos could facilitate future missions to Deimos that would not only expand our understanding of the Martian system, but could complement the Phobos-centric sample return mission being undertaken by *MMX*.

The dynamic environment at Deimos is challenging from a mission design standpoint. The body is massive enough that its gravity obviously must be taken into account, but not so massive that it allows for a large stable gravity well. Large portions of the orbital tradespace about Deimos are quickly destabilized by the gravitational potential of Mars or other perturbations. Mission design at Deimos is very limited by Martian perturbations alone, and requires a careful selection of a stable science orbit.

1.2.1 Previous Studies of the Deimos System Dynamics

A number of proposed missions or concept studies have discussed studying Deimos via an orbiter or flybys, but a large majority have not performed detailed studies of the dynamics near Deimos. This subsection will summarize the state of the art research in the dynamics about Deimos specifically.

In the late 1980s and early 1990s, multiple theses at the Air Force Institute of Technology (AFIT) focused on finding stable periodic orbits about both Phobos and Deimos. The first, written by Jansson in 1989, focused on the use of Poincaré surfaces of section, and computed a family of planar, retrograde orbits about each body [21]. The second thesis, by Luria in 1990, continued the work by Jansson and applied numerical continuation methods in order to generate and evaluate large numbers of retrograde orbits in the vicinity of Deimos. The Floquet multipliers were also computed to study the dynamic stability of these orbits [22].

These two works from AFIT were later summarized by Wiesel and the sensitivities of the orbits were numerically examined. Wiesel studied the effect of moving from the circular restricted three-body problem into a model that took into account the non-zero eccentricity of Deimos about Mars and identified regions of long-term stability for retrograde orbits at Deimos that are resilient to injection errors [23].

In the late 1990s, Rahe et al. proposed a spacecraft utilizing electric thrust that would loiter near Phobos and Deimos in an orbit synchronized with the period of each moon about Mars. The authors found that such orbits could fly at altitudes of several kilometers over the surface of both moons, but the dynamics of each system were not explored in detail [24].

In support of the Mars-Moon Exploration Reconnaissance and Landed Investigation (MERLIN) mission proposed to the NASA Discovery Program, Guo studied the design and coverage of a set of inclined retrograde orbits in the vicinity of Deimos in 2012. These orbits varied between 300 km to 50 km away from Deimos, and a "walk-in" strategy was developed for transferring from the high-altitude to low-altitude orbits. Guo called this family of trajectories "G-3D" for "general three-dimensional orbits" [25].

The Scheeres book *Orbital Motion in Strongly Perturbed Environments* dedicated a chapter to studying the dynamics at Deimos as an example of an interesting problem which has similarities to the more well-studied dynamics at Phobos. This chapter explored two unstable prograde families about Deimos, and the more stable retrograde

family. Zero-velocity curves were also calculated about the body, and the motion was estimated via both the Hill model and the Clohessy-Wiltshire equations of unforced relative motion [26].

The original PSDS3 report for *Chariot* utilized a retrograde relative orbit with Deimos with a semi-major axis of 115 km. Coverage was computed for this orbit over a 30 day science phase [1].

The *DePhine* proposal has yielded some of the most important previous work on stable trajectories in the Deimos vicinity. Spiridonova et al. [27] and Oberst et al. [15] both describe the utilization of retrograde orbits about Deimos that are inclined out of the Deimos equatorial plane. The focus of the work is generally on very low altitude orbits, in the 8 - 12 km range, but Spiridonova et al. does provide some numerical stability analyses across the larger tradespace of Deimos trajectories [27].

Motivated by the JAXA *MMX* mission, a number of more analytical analyses of the long-term stability of trajectories near small bodies in the circular restricted three-body problem have been performed in recent years. Two of the more notable examples include Baresi et al. [28] and Nishimura et al. [29]. Both of these works sought to study the long-term evolution and stability of inclined distant retrograde orbits via dynamical systems theory, which could be applied to the Mars - Deimos problem.

Again motivated by the upcoming *MMX* mission, Ikeda et al. [17] has provided some of the most notable academic literature on planning operations in a close-proximity orbit to Phobos or Deimos. The paper in question is focused on Phobos given the focus of *MMX*, but many of the concepts discussed can be applied to Deimos as well. For example, the transfer strategy between distant retrograde orbits that is developed for Phobos by Ikeda et al. can also be applied to Deimos. The paper also performs a number of numerical sensitivity studies of retrograde orbits at Phobos, the methodology of which could be applied to Deimos.

1.2.2 Improvements Upon the State of the Art

This thesis builds upon the works discussed previously and advances the state of the art for science orbit design and proximity-operations near Deimos. Specifically, Deimos surface coverage is studied for the entire orbital tradespace in order to design a science orbit that maximizes coverage for a given set of science requirements. For any given mission, a science orbit is designed based on a large number of factors, including spacecraft technical resource budgets, science requirements, and instrument selection, but the methodology shown in this work for optimizing a science orbit should apply to any hypothetical remote sensing mission at Deimos.

Additionally, the coverage analysis is combined with numerical stability analyses performed again across the entire orbital tradespace. The combination of these two analyses allows for future mission design at Deimos that can quickly take into account both the coverage and stability metrics for close-proximity orbits about Deimos.

1.2.3 Thesis Organization

Beyond this introduction, this thesis is organized into four additional chapters.

Chapter 2: Mathematical Frameworks

The circular restricted three-body problem (CRTBP) is introduced, and the equations of motion are derived. This set of equations of motion will serve as the core dynamics that govern the Mars - Deimos system in this thesis.

A method of STM-based targeting in the CRTBP is demonstrated that will later be used to generate families of periodic orbits. An index for quantifying the stability of periodic orbits in the CRTBP that utilizes the eigenvalues of the STM is defined. Targeting via the pseudo-inverse of a numerical Jacobian matrix is also demonstrated, which will allow for more complicated targeting in the ephemeris model.

Planetary constants and spherical harmonic models associated with the Deimos system are defined, and the force model for propagations that take place in the ephemeris model is summarized.

Chapter 3: Periodic and Quasi-Periodic Orbits at Deimos

The dynamics of the Mars - Deimos system are examined in the Circular Restricted Three-Body Problem. With this set of assumptions, periodic orbits about Deimos are generated. The linear stability and dynamics of these periodic orbits is explored.

Quasi-satellite orbits are introduced, and visualized in multiple frames. The benefits of quasi-satellite orbits for remote sensing observations are discussed.

Chapter 4: Mission Analysis at Deimos

Theoretical and numerical studies on the stability of quasi-satellite orbits about Deimos are performed and discussed. Science orbits for a potential mission to Deimos with a notional set of instruments and science requirements are generated and visualized.

Long-term coverage analyses of some selected science orbits are performed with more complex solar constraints. Numerical studies on the sensitivities of initial conditions for distant retrograde orbits about Deimos are performed in order to inform CONOPS and mission operations.

Chapter 5: Conclusions and Future Work

The work is summarized, and recommendations for future work are made.

2. MATHEMATICAL FRAMEWORKS

2.1 Circular Restricted Three-Body Problem

The Circular Restricted Three-Body Problem (CRTBP) is a simplification of the general three-body problem which has no analytical solution. The general three-body problem, and more simplified models based upon it, has been studied for centuries by giants of celestial mechanics such as Euler, Lagrange, Jacobi, Hill, and Poincaré, as well as a number of more modern researchers [30, 31].

While the general mathematical framework of the three-body problem is derived from the gravitational laws of Newton, Euler was the first to apply the key "restriction" relevant to trajectory design, that the third body could be assumed to be massless when compared to the other two. He also approached the three-body problem in a rotating frame, which is the standard method for analyzing the problem today [30,31]. Hill and Poincaré would go on to study periodic orbits in the restricted three-body problem, and this work gave rise to the later more extensive numerical exploration of periodic orbits in the restricted problem by Hénon [31–36].

The three-body problem models the motion of a body (denoted P3) under the gravitational influence of two other bodies (denoted P1 and P2). The motion of P3 via Newton's Second Law is given as a function of the masses m_1 and m_2 and their relative positions in Equation 2.1.

$$m_3\ddot{\overline{r_3}} = -G\frac{m_3 m_1}{|(\overline{r_3} - \overline{r_1})|^3}(\overline{r_3} - \overline{r_1}) - G\frac{m_3 m_2}{|(\overline{r_3} - \overline{r_2})|^3}(\overline{r_3} - \overline{r_2}) \tag{2.1}$$

The problem can be simplified by making a number of assumptions:

1. m_3 is much less massive than m_1 and m_2. As a result, the motion of m_1 and m_2 is not affected by m_3.

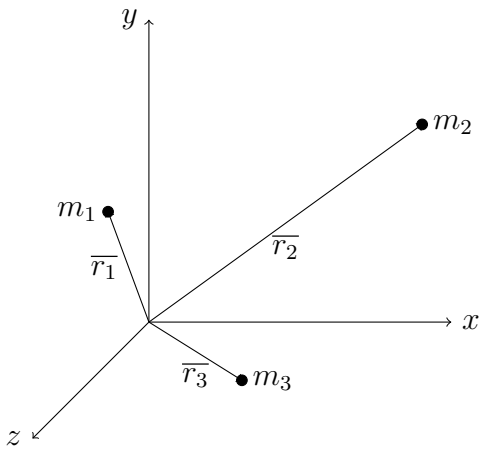

Figure 2.1. The general three-body problem.

2. m_1 and m_2 is an isolated two-body system.

3. m_1 and m_2 move on circular orbits about their mutual barycenter.

These assumptions allow us to simplify the problem, and re-write it using a rotating frame in the orbital plane of m_1 and m_2. This assumption set is commonly referred to as the Circular Restricted Three-Body problem. This re-drawn setup is shown in Figure 2.2.

Re-writing Equation 2.1 based on the notation in this rotating frame, the motion of m_3 with respect to the barycenter can be written as:

$$m_3\ddot{\overline{\rho}} = -G\frac{m_3 m_1}{|\overline{D}|^3}\overline{D} - G\frac{m_3 m_2}{|\overline{R}|^3}\overline{R} \tag{2.2}$$

Next, the mass, distance, and time parameters are non-dimensionalized. Note that in the following notation the bold **G** represents the dimensional Newton's Gravitational Constant, while the non-bold G represents the non-dimensionalized constant.

$$l^* = l_1 + l_2 \tag{2.3}$$

$$m^* = m_1 + m_2 \tag{2.4}$$

$$t^* = \sqrt{\frac{(l^*)^3}{\mathbf{G}m^*}} \tag{2.5}$$

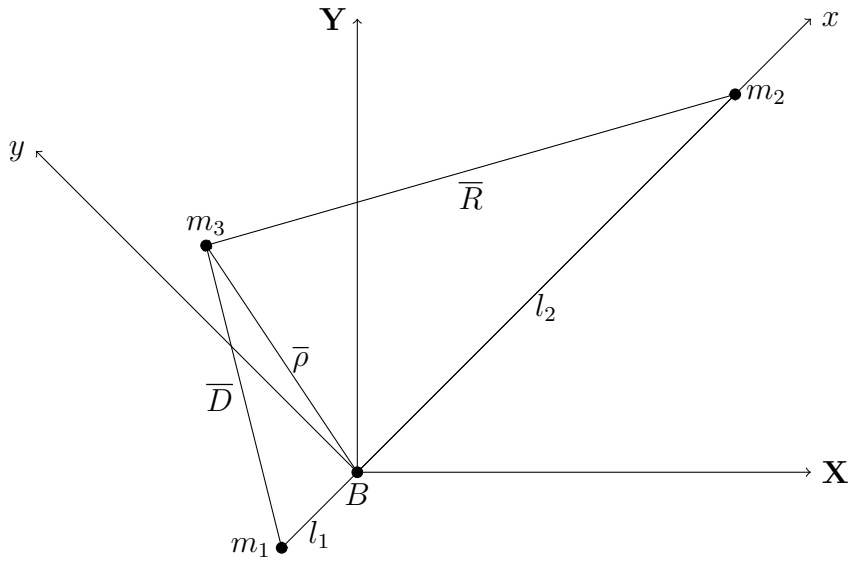

Figure 2.2. The three-body problem redrawn with CRTBP assumptions.

$$\mu = \frac{m_2}{m^*} \tag{2.6}$$

$$G = \frac{\mathbf{G}}{l^3} m^* t^{*2} \tag{2.7}$$

$$\tau = \frac{t}{t^*} \tag{2.8}$$

$$\overline{r} = \frac{\overline{R}}{l^*} \tag{2.9}$$

$$\overline{d} = \frac{\overline{D}}{l^*} \tag{2.10}$$

$$r = |\overline{r}| \tag{2.11}$$

$$d = |\overline{d}| \tag{2.12}$$

Using these non-dimensional quantities, the dimensional expression in Equation 2.2 can be rewritten as:

$$\frac{d^2\overline{\rho}}{d\tau^2} = -(1-\mu)\frac{\overline{d}}{d^3} - \mu\frac{\overline{r}}{r^3} \tag{2.13}$$

Integrating this equation and isolating the x, y, and z components yields:

$$\ddot{x} - 2n\dot{y} - n^2 x = -\frac{(1-\mu)(x+\mu)}{d^3} - \frac{(\mu)(x-1+\mu)}{r^3} \tag{2.14}$$

$$\ddot{y} + 2n\dot{x} - n^2 y = -\frac{(1-\mu)(y)}{d^3} - \frac{(\mu)(y)}{r^3} \tag{2.15}$$

$$\ddot{z} = -\frac{(1-\mu)(z)}{d^3} - \frac{(\mu)(z)}{r^3} \tag{2.16}$$

In the non-dimensional case, the mean motion of the rotating frame, n, simplifies to equal one. This is demonstrated in Equation 2.17 using the notation of $\mathbf{n}$ as the dimensional mean motion and n as the non-dimensional mean motion.

$$n = \mathbf{n}t^* = \sqrt{\frac{\mathbf{G}m^*}{l^{*3}}}\sqrt{\frac{l^{*3}}{\mathbf{G}m^*}} = 1 \tag{2.17}$$

With the simplification of $n = 1$, the equations of motion in Equations 2.14 - 2.16 reduce to:

$$\ddot{x} - 2\dot{y} - x = -\frac{(1-\mu)(x+\mu)}{d^3} - \frac{(\mu)(x-1+\mu)}{r^3} \tag{2.18}$$

$$\ddot{y} + 2\dot{x} - y = -\frac{(1-\mu)(y)}{d^3} - \frac{(\mu)(y)}{r^3} \tag{2.19}$$

$$\ddot{z} = -\frac{(1-\mu)(z)}{d^3} - \frac{(\mu)(z)}{r^3} \tag{2.20}$$

This formulation is the classical set of equations of motion for the Circular Restricted Three-body Problem. The equations of motion can also be re-written using a pseudo-potential U^*. This pseudo-potential based formulation will be utilized in targeters later.

$$U^* = \frac{(1-\mu)}{d} + \frac{\mu}{r} + 0.5(x^2 + y^2) \tag{2.21}$$

$$\ddot{x} - 2\dot{y} = \frac{\partial U^*}{\partial x} \tag{2.22}$$

$$\ddot{y} + 2\dot{x} = \frac{\partial U^*}{\partial y} \tag{2.23}$$

$$\ddot{z} = \frac{\partial U^*}{\partial z} \tag{2.24}$$

2.2 Targeting Periodic Orbits via the State Transition Matrix

The State Transition Matrix (STM) describes the partial derivatives of the states at some arbitrary time t_2 with respect to the states at an earlier time t_1.

As an example of a state transition matrix, the partial derivatives of a final state vector for a simple 2D problem in the XY plane, $[x, y, \dot{x}, \dot{y}]$ can be described with respect to the initial state vector $[x_0, y_0, \dot{x}_0, \dot{y}_0]$ via the STM:

$$\phi = \begin{bmatrix} \frac{\partial x}{\partial x_0} & \frac{\partial x}{\partial y_0} & \frac{\partial x}{\partial \dot{x}_0} & \frac{\partial x}{\partial \dot{y}_0} \\ \frac{\partial y}{\partial x_0} & \frac{\partial y}{\partial y_0} & \frac{\partial y}{\partial \dot{x}_0} & \frac{\partial y}{\partial \dot{y}_0} \\ \frac{\partial \dot{x}}{\partial x_0} & \frac{\partial \dot{x}}{\partial y_0} & \frac{\partial \dot{x}}{\partial \dot{x}_0} & \frac{\partial \dot{x}}{\partial \dot{y}_0} \\ \frac{\partial \dot{y}}{\partial x_0} & \frac{\partial \dot{y}}{\partial y_0} & \frac{\partial \dot{y}}{\partial \dot{x}_0} & \frac{\partial \dot{y}}{\partial \dot{y}_0} \end{bmatrix}$$

The process of targeting is adjusting states or parameters at some point in time in order to achieve a set of desired states or parameters at a later point in time. If the state transition matrix can be computed, the benefit of this matrix to the process of targeting is clear: it provides a mapping of states at one point in time to another point in time.

Using the example of a planar problem in the XY plane again, a change in the future state x can be written as the sum of partial values multiplied by changes in the initial state:

$$\delta x = \frac{\partial x}{\partial x_0}\delta x_0 + \frac{\partial x}{\partial y_0}\delta y_0 + \frac{\partial x}{\partial \dot{x}_0}\delta \dot{x}_0 + \frac{\partial x}{\partial \dot{y}_0}\delta \dot{y}_0 \tag{2.25}$$

For a linear system, this expression is exactly correct. For a nonlinear system, such as the CRTBP, it provides a linearized approximation which may be close to correct depending on the dynamics of the system and the time between t_0 and t.

One of the challenges for utilizing the STM in targeting is calculating the values of the partial derivatives. In the CRTBP, this is commonly done numerically via finite differencing, or by integrating the STM in conjunction with the equations of motion.

Integrating a 6 dimensional state and a 6x6 STM involves integrating 42 nonlinear equations simultaneously whereas for the finite differencing method, it is only integrating the 6 equations describing the state multiple times for each partial derivative needed. Either way will work in a numerical targeter, but there may be computational performance differences depending on how many partial derivatives are necessary for the targeter in question.

2.2.1 Finite Differencing

For finite differencing, the ultimate goal is to estimate the values of the STM without integrating the full matrix. This can be done by making a small perturbation to the initial state in question and observing the effect on the final state in question.

For central differencing, which requires two integrations, the partial derivative value can be approximated as the following, where δ is some small value, and x is the variable being changed.

$$\frac{\partial f}{\partial x} = \frac{f(x+\delta) - f(x-\delta)}{2\delta} \tag{2.26}$$

This process would be repeated for each dimension of f and each dimension of x for which a partial derivative is required. Again, the benefit of this method is that the full STM does not need to be integrated. For a very simple targeter (for example, one that varies one initial variable in order to hit a target value of one final variable), it is possible to only estimate the partials required instead of the full STM, which can be more computationally efficient. However, it is very much problem-dependent.

2.2.2 STM Integration

For integrating the STM in order to obtain the full STM at any given point, the integration takes the form:

$$\dot{\phi} = A\phi \tag{2.27}$$

$$A = \begin{bmatrix} 0 & 0 & 0 & 1 & 0 & 0 \\ 0 & 0 & 0 & 0 & 1 & 0 \\ 0 & 0 & 0 & 0 & 0 & 1 \\ U^*_{XX} & U^*_{XY} & U^*_{XZ} & 0 & 2 & 0 \\ U^*_{YX} & U^*_{YY} & U^*_{YZ} & -2 & 0 & 0 \\ U^*_{ZX} & U^*_{ZY} & U^*_{ZZ} & 0 & 0 & 0 \end{bmatrix} \tag{2.28}$$

Where U^*_{XX} is defined as $\dfrac{\partial^2 U^*}{\partial x \partial x}$, and the other partials are defined similarly.

For this formulation, the initial conditions for the STM, ϕ_0 are defined as a 6x6 identity matrix. This comes from the definition of the STM itself: when the final time t_2 is equal to the start time t_1, there is exactly a 1:1 ratio between changes in the initial state and changes in the final state - the state vectors are the exact same. This formulation allows for the integration of all 36 STM elements in concurrence with the integration of the states.

2.2.3 STM-Based Targeting for Periodic Orbits

Once the elements of the STM have been computed, they can be utilized to target periodic orbits in the CRTBP. If a system is linear, the change in a final state as a function of changes in an initial state can be written via the STM as:

$$\delta\overline{X_f} = \phi * \delta\overline{X_0} \tag{2.29}$$

If this system is nonlinear, this formulation is not exactly correct, but it is often close over relatively short propagation times. By taking the inverse of the STM, the reverse problem can be examined: the predicted change in an initial state required to yield a desired change in the final state.

$$\delta\overline{X_0} = \phi^{-1} * \delta\overline{X_f} \tag{2.30}$$

This formulation is useful for any sort of state-based targeting. Given that the STM is a linearized approximation of the partial derivatives, this formulation is often

used in an iterative fashion, making repeated adjustments to the initial state until eventually the final state has converged to the desired values.

For targeting periodic orbits, a common method is to start with an initial condition on the X-axis and adjust the initial velocity $\dot{Y}_0$ such that the next X-axis crossing is perpendicular.

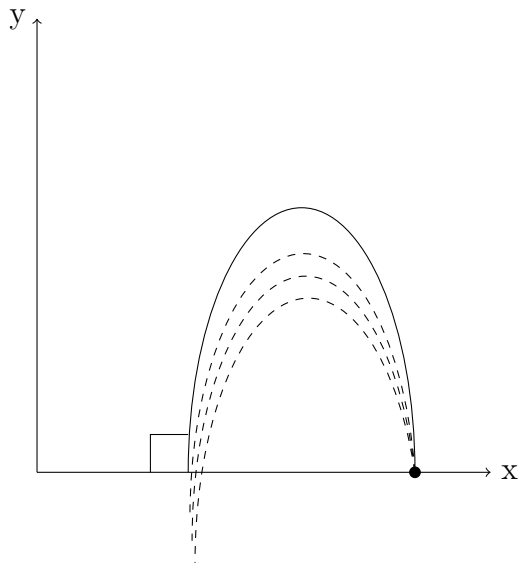

Figure 2.3. A method for targeting periodic orbits in the CRTBP.

This method is effective because the dynamics are mirrored about the X-axis. So if a trajectory leaves and then re-crosses the X-axis both via perpendicular crossings, a continued propagation will mirror the first propagation across the X-axis and complete a full periodic trajectory [37, 38]. This observation is often referred to as the "mirror theorem".

The method of computing periodic orbits by searching for perpendicular X-axis crossings and adjusting initial conditions via estimated partial derivatives was demonstrated extensively by Hénon in his numerical explorations of the restricted problem [34, 35].

2.3 Periodic Orbit Stability Index

There are a number of methods for quantifying the stability of periodic orbits in the CRTBP. For the analysis in this thesis, the stability characteristics are determined via the monodromy matrix, or the state transition matrix as defined in Section 2.2 evaluated after one full period of a periodic orbit.

After one full period, the eigenvalues of the monodromy matrix can be computed. Via Lyapunov's Theorem, there will be two eigenvalues equal to one, and two additional reciprocal pairs. For the trajectories analyzed in this thesis, the four non-unity eigenvalues all exist on the unit circle, and the stability criteria can be determined via a combination of the reciprocal pairs.

For the analysis in this thesis, there are three indices developed for each orbit based on the eigenvalues of the monodromy matrix. These three indices jointly determine the stability of the periodic orbit. The three stability indices are defined as follows:

$$\nu_1 = 0.5(\lambda_1 + \lambda_2) \tag{2.31}$$

$$\nu_2 = 0.5(\lambda_3 + \lambda_4) \tag{2.32}$$

$$\nu_3 = 0.5(\lambda_5 + \lambda_6) \tag{2.33}$$

Where (λ_1, λ_2), (λ_3, λ_4), and (λ_5, λ_6) are the three pairs of reciprocal eigenvalues.

For this convention, an index between -1 and +1 in all three of the indices signifies stability in the linear sense. If any one of the three indices has a magnitude greater than one, the periodic orbit is considered unstable. Given that the imaginary components cancel when adding the two reciprocal pairs, using this notation there is no differentiation between asymptotic stability (which occurs with a real eigenvalue with a magnitude less than 1) and Lyapunov stability (which occurs with an eigenvalue on the complex unit circle) [29].

2.4 Numerical Targeting in GMAT

With a simplified dynamics model, targeting via the state transition matrix as described in Section 2.2 works quite well. However, moving to the ephemeris model, it can become computationally difficult to propagate the station transition matrix. The tool of choice for ephemeris propagation and targeting in this thesis is the General Mission Analysis Tool (GMAT), a validated toolset developed by the Goddard Space Flight Center, and used on a number of operational missions [39]. For this analysis in GMAT, targeting for computing periodic orbits, performing maneuvers, and stationkeeping is performed via a Newton-Raphson differential corrector with partial derivatives computed via finite differencing. The use of finite differencing instead of the analytical evaluation of derivatives makes it a quasi-Newton method.

Generally, a Newton-Raphson method is an iterative root-finding method such that:

$$x_{n+1} = x_n - \frac{f(x_n)}{f'(x_n)} \tag{2.34}$$

In this case, f is a function of variables x, and represents the set of achieved offsets from a set of desired parameter values. The Newton-Raphson solver seeks to find a set of variables x such that each offset is zero (meaning that the variables yield the desired parameter values).

For a multi-dimensional targeter where multiple parameters are varied and targeted simultaneously, a Jacobian matrix is used instead of a scalar function evaluation.

$$J = \begin{bmatrix} \dfrac{\partial f_1}{\partial x_1} & \cdots & \dfrac{\partial f_1}{\partial x_k} \\ \vdots & \ddots & \vdots \\ \dfrac{\partial f_k}{\partial x_1} & \cdots & \dfrac{\partial f_k}{\partial x_k} \end{bmatrix} \tag{2.35}$$

$$\begin{bmatrix} x_1 \\ \vdots \\ x_k \end{bmatrix}_{n+1} = \begin{bmatrix} x_1 \\ \vdots \\ x_k \end{bmatrix}_{n} - J^{-1} \begin{bmatrix} f_1(x_1) \\ \vdots \\ f_k(x_k) \end{bmatrix} \tag{2.36}$$

Note here that if all 6 initial states are varied and all 6 final states are targeted, the Jacobian matrix here is equivalent to the STM. The update equation formulated in Equations 2.35 and 2.36 works for targeting where the number of variables and constraints are equal and the Jacobian matrix can be easily inverted.

When the number of variables and constraints are not equal, the Jacobian is not invertible, and GMAT calculates a pseudo-inverse of the Jacobian [1] :

If the number of variables is greater than the number of constraints (the problem is underconstrained):

$$J^{-1} \approx J^T(JJ^T)^{-1} \tag{2.37}$$

If the number of variables is less than the number of constraints (the problem is overconstrained):

$$J^{-1} \approx (J^T J)^{-1}J^T \tag{2.38}$$

This method of using pseudo-inverses in order to invert a non-square Jacobian allows for targeting of desired parameters when the problem is under or overconstrained. This benefit can be very useful when working in an ephemeris model rather than a simplified dynamics model as the targeting is often more complex than in the CRTBP.

2.5 Ephemeris Model Dynamics and Planetary Constants

For evaluations in this thesis that involve propagating a spacecraft in the ephemeris model, the set of constants and force model was standardized across runs to ensure consistency. The planetary ephemerides and GM values are based on the DE431 [40] and MAR097 [41] ephemeris files for the solar system and Martian system respectively.

For Deimos specifically, the GM value is based on MAR097, but there is also a spherical harmonic model developed by Rubincam, Chao, and Thomas [42]. For

[1]Some of the mathematical references in the GMAT documentation have been a work in progress for years, and this information is not found in the published documentation. However, the open source nature of the project allows researchers to examine the C++ source code itself to confirm the pseudo-inverse implementation.

this model, it is important to note that the spherical harmonic terms have not been refined based on radiometric tracking data, but via a Deimos shape model and an assumption of uniform density. Tracking data that would allow for a Deimos spherical harmonic model to be refined simply does not exist because there have been no close-approaches of Deimos by any spacecraft. There are relatively high uncertainties on both the Deimos GM value and the spherical harmonic values, which is discussed in Section 3.2.

Ephemeris propagations were performed with the 4x4 spherical harmonic model developed by Rubincam, Chao, and Thomas [42] and point masses for Mars, Phobos, and the Sun. The Deimos body frame is modeled via the conventions of the 2017 IAU Working Group [43]. An alternate dynamic setup could have utilized a Martian spherical harmonic model and a Deimos point mass. This is likely a more appropriate model for trajectories that are further away from Deimos, while the Deimos spherical harmonic model and Mars point mass is more appropriate for close-proximity trajectories. The astrodynamics packages used in this research did not support propagation with multiple spherical harmonic models simultaneously, so one setup needed to be chosen. A future analysis that takes into account both Mars and Deimos spherical harmonics could be a useful extension of this work.

A comparison of the acceleration due to the Mars and Deimos GMs and Mars and Deimos J2 perturbations as a function of the distance from Deimos is shown in Figure 2.4. It should be noted that the value for the Mars and Deimos J2 acceleration should be considered to be an upper bound. The actual value for the acceleration in a spherical harmonic model is a function of the latitude and longitude with respect to the body-fixed frame of each body. In comparing the spherical harmonic models for Mars and Deimos, the J2 acceleration for Deimos outweighs that of Mars inside approximately 25 km, and the J2 for Mars outweighs the J2 of Deimos outside this distance.

Given the sensitivity of some of these orbits, a basic spherical solar radiation pressure model was added based on notional values for area to mass ratio and coefficient

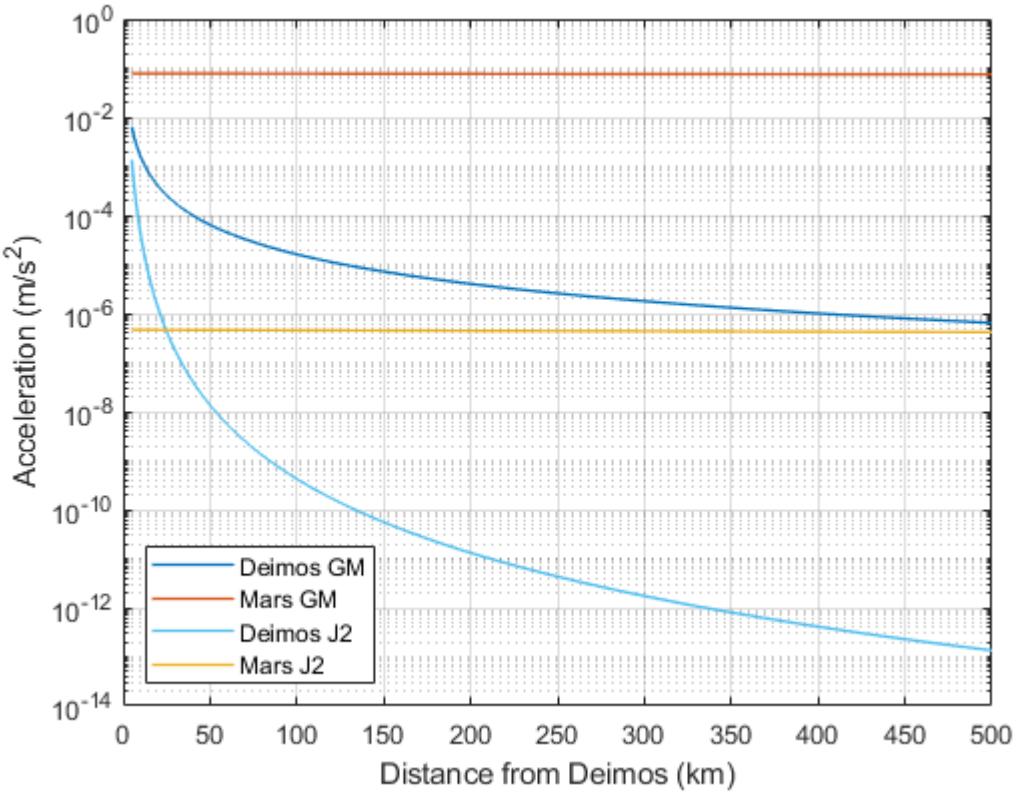

Figure 2.4. Accelerations due to Mars and Deimos as a function of distance from Deimos.

of reflectivity. These SRP parameters are obviously spacecraft-dependant, but they do not have a large effect on the trajectories evaluated in this thesis. The notional values here are realistic for a small to medium-sized interplanetary spacecraft.

All propagations in the ephemeris model are performed with a starting epoch of Oct 1, 2025, 00:00:00 UTC, which is chosen to correspond with an arbitrary Earth - Mars transfer window arrival time in the mid-2020s.

Table 2.1. Spacecraft Force Model and Dynamic Setup

Force / Parameter	**Details**
Spherical Harmonic	Deimos 4x4
Point Mass	Mars, Phobos, Sun
Solar Radiation Pressure	Spherical Model
Area / Mass Ratio	0.0278
Coefficient of Reflectivity	1.8
Epoch	Oct 1, 2025, 00:00:00 UTC

3. PERIODIC AND QUASI-PERIODIC ORBITS AT DEIMOS

The dynamics of the Deimos system are very challenging when compared to some larger planetary bodies. The Hill radius of Deimos, or the radius inside which the gravitational potential of Deimos is dominant, is approximately 25 km [26]. Previous studies of trajectories near small bodies have shown that trajectories outside approximately half of the Hill radius tend to escape over time due to outside perturbations [26,44]. The Deimos shape model used in this analysis is the model developed by P.C. Thomas in 2000, with principal axes measuring 15.9 km x 12.6 km x 11.1 km [45].

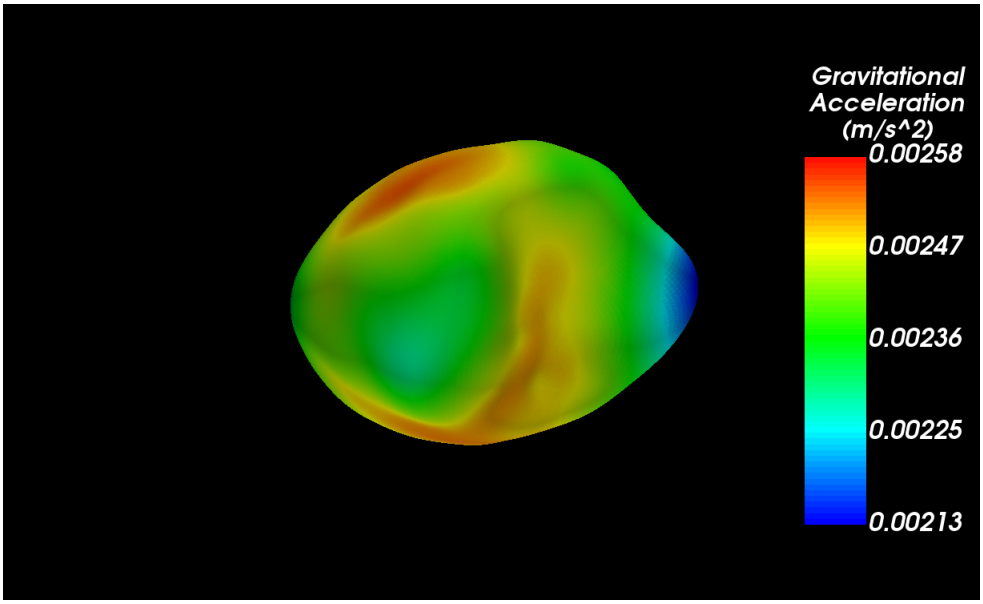

Figure 3.1. The Deimos shape model developed by Thomas (2000) [45]. Visualized in the Small Body Mapping Tool [46].

If the Hill radius is assumed to be constant about the body, this leaves less than 7 km above the surface where stable, Keplerian-like orbits *may* exist. Given these extreme constraints on orbits about Deimos, the best way to analyze the problem is within the framework of the Mars - Deimos three-body problem.

3.1 Mars - Deimos Rotating Frame Definition

In the Mars - Deimos three-body problem, propagations are often viewed in a Mars - Deimos rotating frame. This frame, shown in Figure 3.2, is defined such that the X-axis is along the Mars - Deimos radial vector, the Z-axis is aligned with the Deimos angular velocity vector, and the Y-axis completes the right-handed system. With the CRTBP assumption of a circular orbit of Deimos about Mars, the Y-axis is also perfectly aligned with the Deimos velocity vector, but when used in an ephemeris model with the actual orbit of Deimos, this is not the case. Note that in this thesis, the coordinate frame is centered at the Deimos center of mass whereas in Figure 2.2, the rotating frame was centered at the mutual barycenter of the primary and secondary bodies. This is done for ease of interpretation when examining trajectories in the Deimos vicinity.

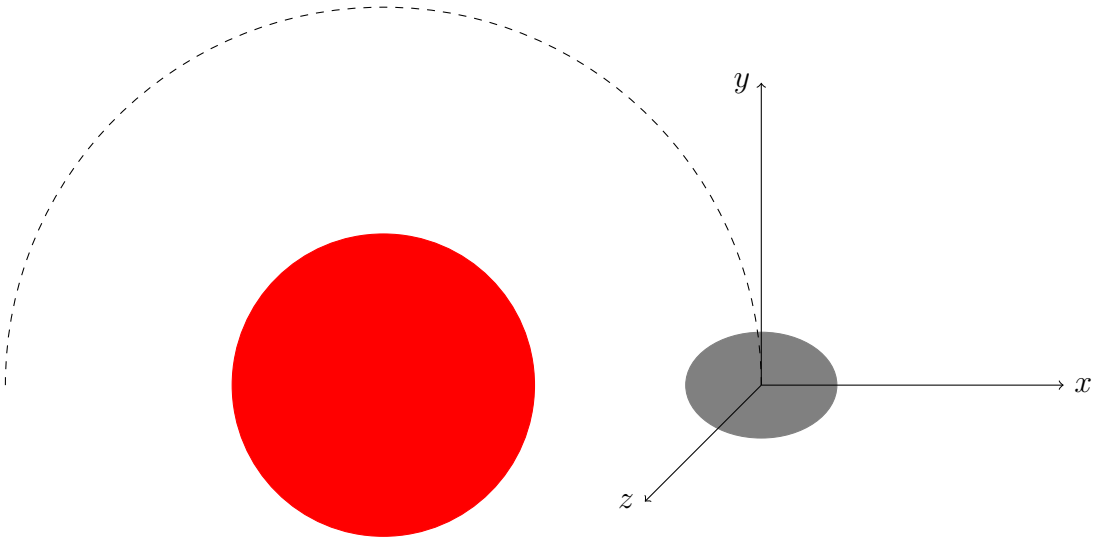

Figure 3.2. The Deimos-centered Mars - Deimos rotating frame. Not to scale.

3.2 Lagrange Points at Deimos

A logical first step for trajectory design in the three-body problem is to examine the Lagrange points in the CRTBP. For Deimos, the L1 and L2 Lagrange points exist at approximately +/- 21 km along the Mars - Deimos radial vector. This is approximately 13 km above the surface of Deimos.

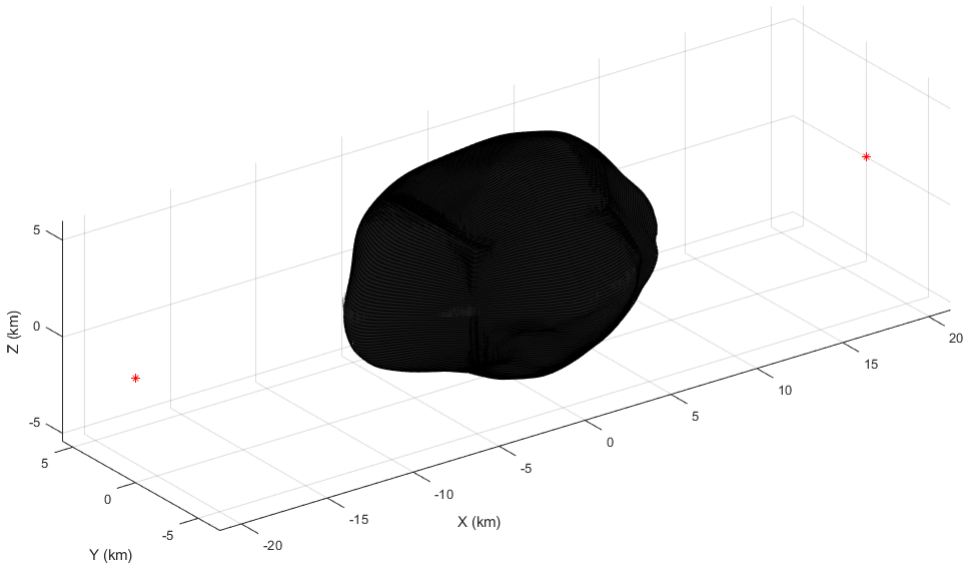

Figure 3.3. The Mars - Deimos L1 and L2 Lagrange points with respect to the shape model in the Mars - Deimos rotating frame.

This distance could theoretically allow for very small halo orbits or other families at the Mars - Deimos L1 or L2 points. However, these were not considered for a number of reasons:

First, periodic orbits about Lagrange points are inherently very sensitive. This can usually be managed with small stationkeeping burns, however, for a body like Deimos with significant uncertainties on mass properties, the location of the Lagrange points themselves are uncertain. Estimates of the mass of Deimos are performed based on ground observations and spacecraft tracking at Mars. However, as previously discussed, there are no spacecraft that make regular close approaches of Deimos, making estimation of parameters difficult.

Modern estimations place uncertainties on the mass of Deimos at anywhere from 7 percent to more than 35 percent [47]. If the upper and lower bounds of Deimos GM estimations are considered, the Lagrange points may actually exist at anywhere between 17.8 km and 24 km away from the center of mass.

As the Lagrange points shift, the corresponding initial conditions for periodic orbits also shift. As such, any mission that baselined halo orbits, or other similar families of L1 or L2-centric trajectories near Deimos would likely need to perform an early phase of GM estimation in a stable orbit before the libration point orbit phase could begin.

In addition to these challenges, there is the more practical consideration that Deimos is tidally locked, meaning that the observation geometry of the spacecraft would be "locked" onto one side of the body. It would of course be possible to make observations of one side before transitioning to the Lagrange point on the other side of Deimos, but it may be more desirable to find a trajectory that can provide global observations without any transitions between orbits.

3.3 Prograde Orbits About Deimos

Very close to Deimos, there are a number of prograde periodic orbits that exist mathematically in the CRTBP. The two families are called the *g* and *g'* families by Hénon [34]. These two families are planar and exist in the Mars - Deimos orbital plane.

While these families may exist mathematically about a Deimos point mass, in reality, many of the members of the *g* family intersect the Deimos surface. A subset of the family near Deimos is shown in Figure 3.4.

For the *g'* family, which bifurcates from the *g* family around an X_0 value of 10 km, the geometry is such that many members of the family do not intersect the Deimos surface. However, all members of the family are extremely unstable and require very tight controls on the initial conditions in order to avoid impacting or leaving the

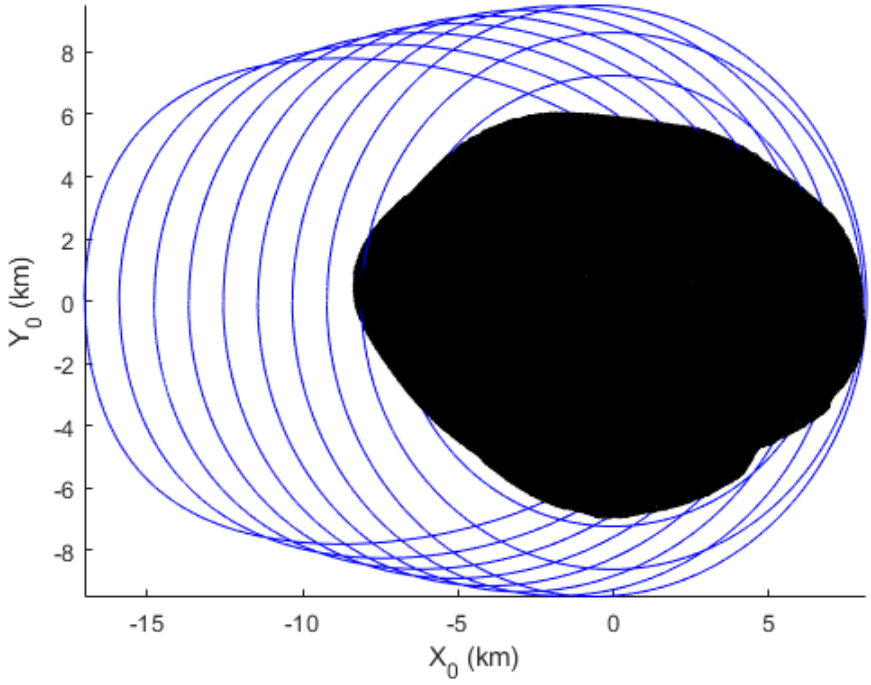

Figure 3.4. The g family of orbits about Deimos in the Mars - Deimos rotating frame.

body. This inherent instability combined with the uncertainties on the Deimos mass described in Section 3.2 means that the use of this family for an actual mission would be extremely challenging.

3.4 Distant Retrograde Orbits

The family of periodic planar retrograde orbits about the secondary body was originally called the f family by Hénon [36] in the circular Hill problem. In the circular Hill problem, the mass of the secondary body is assumed to be "vanishingly small" (to quote Hénon) when compared to that of the primary, i.e. $\mu = 0$. In more recent nomenclature, the members of this family for values of $\mu \neq 0$ have been referred to as distant retrograde orbits (DROs). In this thesis, the terms "distant retrograde orbit" and "f family" will be used interchangeably.

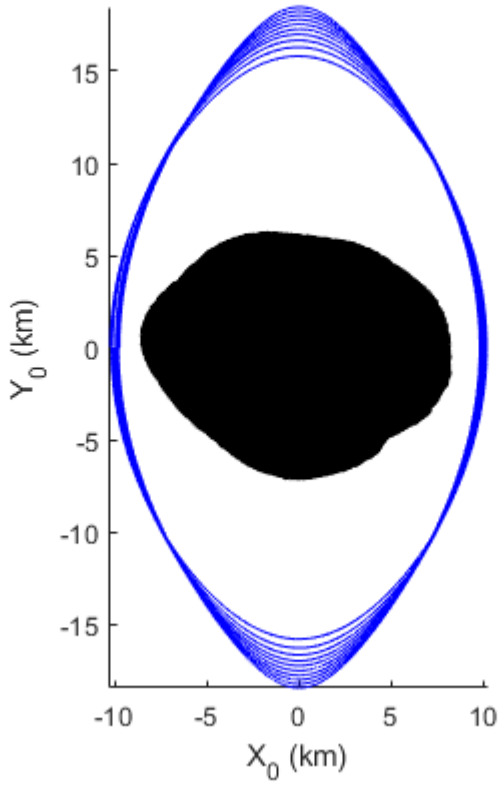

Figure 3.5. The *g'* family of orbits about Deimos in the Mars - Deimos rotating frame.

These orbits lie in the same orbital plane as the secondary body about the primary, which for tidally locked bodies such as Deimos means that they also lie in the Deimos equatorial plane. DROs have long been of interest to mission designers due to their stability when compared to other periodic orbits in the CRTBP [34, 48, 49].

Previous studies on mission design at Deimos have found that distant retrograde orbits (DROs) are the only stable periodic orbits about Deimos [26]. Using the STM-based targeting method described in Section 2.2, the f family about Deimos can be generated in the Mars - Deimos rotating frame.

The f family for X_0 values of 10 km - 100 km is shown in Figure 3.6. Near Deimos, the family appears nearly circular, however, as the family grows, the ratio of the Y-axis amplitude to X-axis amplitude approaches approximately 2:1. The evolution of

this ratio across this subsection of the family is shown in Figure 3.7. The approach towards a 2:1 ratio is expected: as the f family grows, the gravitational potential from Deimos decays, and the relative motion approaches the unforced relative dynamics of two massless objects in two-body orbits with respect to Mars. This 2:1 ratio of along-track vs radial oscillation is seen in the relative motion described by the Clohessy-Wiltshire equations or any number of relative orbital element formulations that describe unforced relative motion [50, 51].

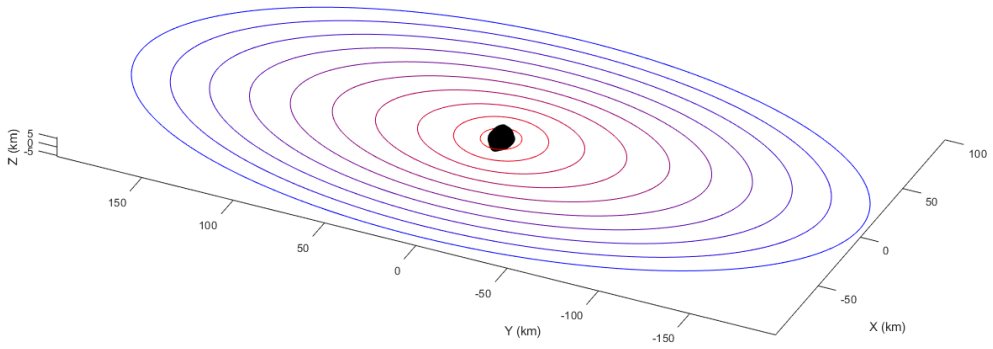

Figure 3.6. The f family of orbits about Deimos in the Mars - Deimos rotating frame.

Another parallel to unforced relative motion is seen when the period of the f family about Deimos is compared to the period of Deimos about Mars. For low-altitude members of the family, where the gravitational force due to Deimos is significant, the orbital period about Deimos can be as low as five hours, significantly shorter than the approximately 30 hour period of Deimos about Mars. However, for larger members of the family, the period of members of the f family asymptotically approaches the period of Deimos about Mars.

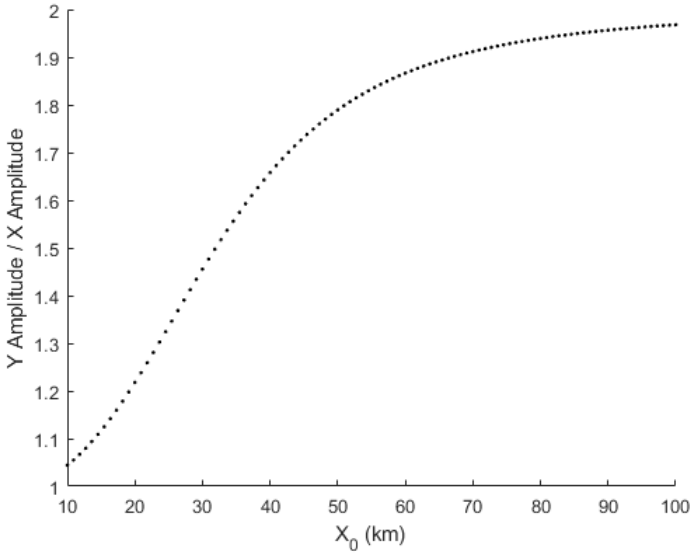

Figure 3.7. Ratio of the Y amplitude to X amplitude as the f family grows.

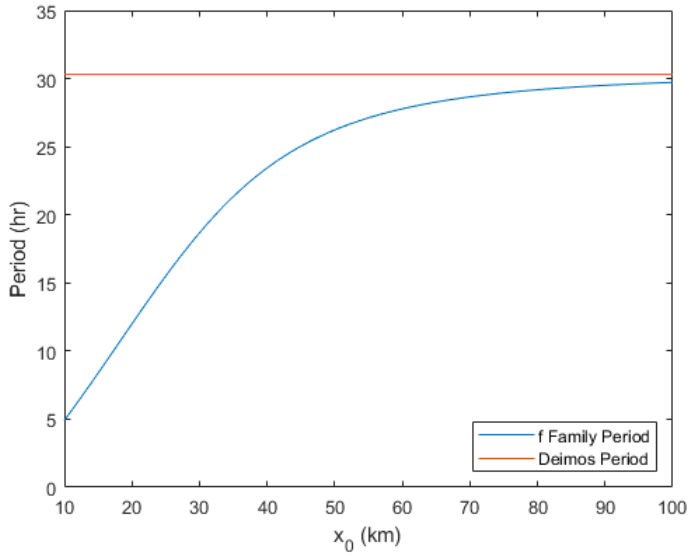

Figure 3.8. Period of the f family of orbits about Deimos compared to the Deimos period about Mars.

Similarly to the 2:1 behavior discussed previously, this occurs as the gravitational force due to Deimos decays. As the family grows, it transitions from a Deimos-

dominated trajectory to a Mars-dominated trajectory perturbed by Deimos, and eventually approaches a behavior where Deimos has little to no effect on the trajectory. For unforced relative motion, which is what the f family approaches as it grows larger, the period of the relative motion is equal to the period of the "chief" object (Deimos in this case) about its primary (Mars).

It is important to note here that this is the period with respect to the Mars - Deimos rotating frame. Given that Deimos is tidally locked, the period is also given with respect to the Deimos body frame. Instead of the phrase "orbital period", some authors in the literature have referred to this apparent motion about the body frame of the secondary body as an "epicycle period", and left the terminology "orbital period" to describe the period about the primary body [16]. For a DRO, the orbital period of a member of the f family *with respect to the primary* will be equal to the orbital period of the secondary body. The period shown in Figure 3.8 is the period with respect to the Deimos body frame, or the epicycle period in the nomenclature of other authors.

The initial conditions solved by the targeter are shown in Figure 3.9. There is an inflection point near an X_0 value of 20 km, representing where the family transitions from inside the L1 and L2 Lagrange points to outside. In generating the f family, initial guesses for the targeter are calculated based on a continuation method using a spline fit of the solved members that have been already generated.

Applying the stability index described in Section 2.3, the three resulting indices are shown in Figure 3.10. This metric shows the mathematical stability of the family of DROs about Deimos. Similar to the initial condition plot in Figure 3.9, there is an inflection point for two of the three indices near the transition from inside the Mars - Deimos L1 and L2 points to outside those points. The third index is constantly equal to one. All three indices have a magnitude less than or equal to one signifying Lyapunov stability across all analyzed members of the family.

While distant retrograde orbits appear to be smooth oval-like shapes when viewed in a rotating frame, in an inertial frame, the motion is more complex. A sample

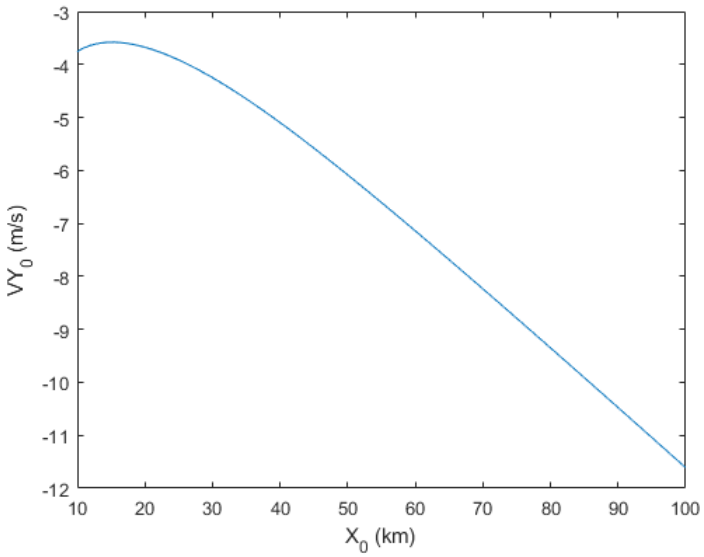

Figure 3.9. Initial conditions for the f family of orbits about Deimos.

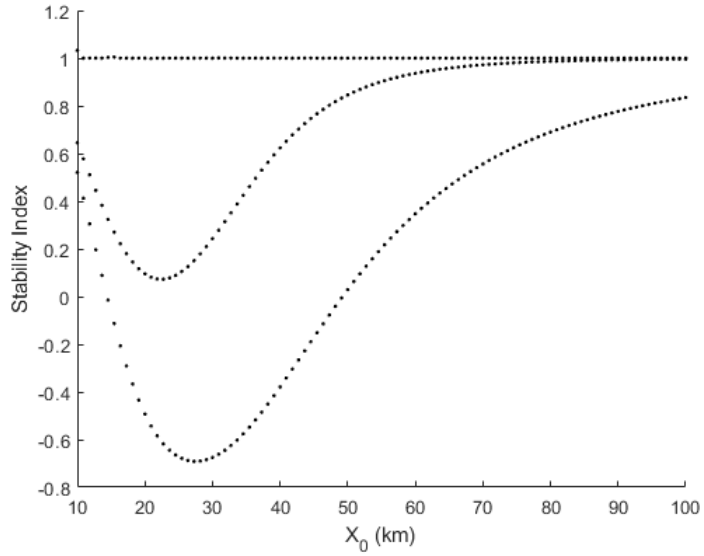

Figure 3.10. Stability index of the f family of orbits about Deimos.

member of the family with an X_0 value of 50 km is shown in a Deimos-centered inertial frame in Figures 3.11 and 3.12.

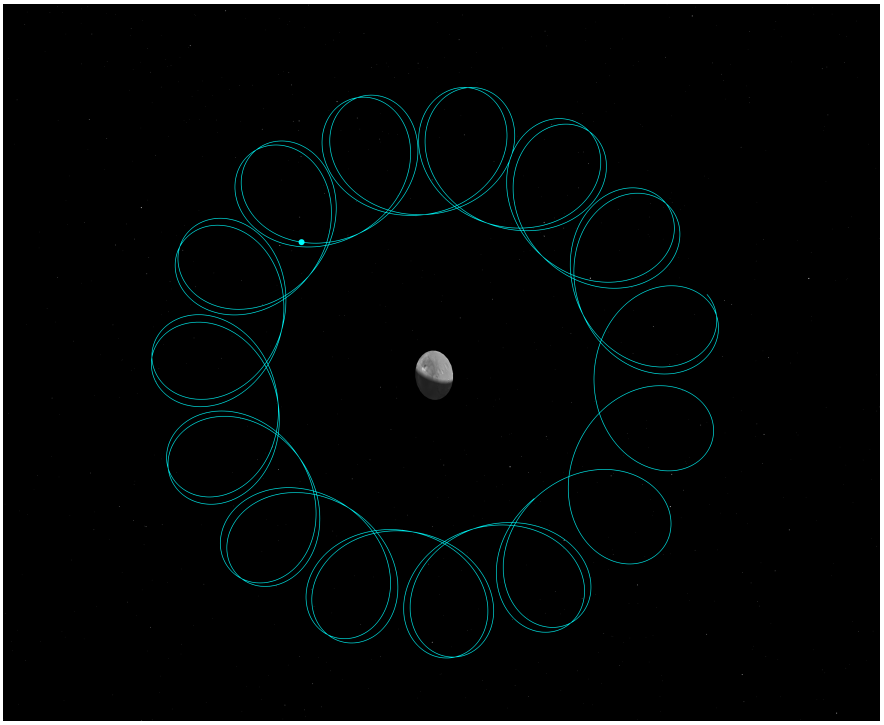

Figure 3.11. Example member of the f family as viewed in the Deimos-centered inertial frame from above.

In inertial space, each trajectory moves about Deimos very slowly, and there are portions of each orbit where the relative inertial motion changes direction each orbit. The motion seen in a rotating or Deimos-fixed frame is primarily driven by the rotation of Deimos underneath the spacecraft rather than the inertial motion of the spacecraft about the Deimos center of mass.

In the example DRO shown in Figures 3.11 and 3.12, each "loop" represents half of a period of the spacecraft about the Deimos body frame (an epicycle using the nomenclature previously discussed). The closest point to Deimos in each loop occurs when the spacecraft crosses the Mars - Deimos radial vector.

Figure 3.12 is the same inertial representation, but from a viewpoint where Mars is visible to demonstrate that the inertial motion lies in the orbital plane of Deimos.

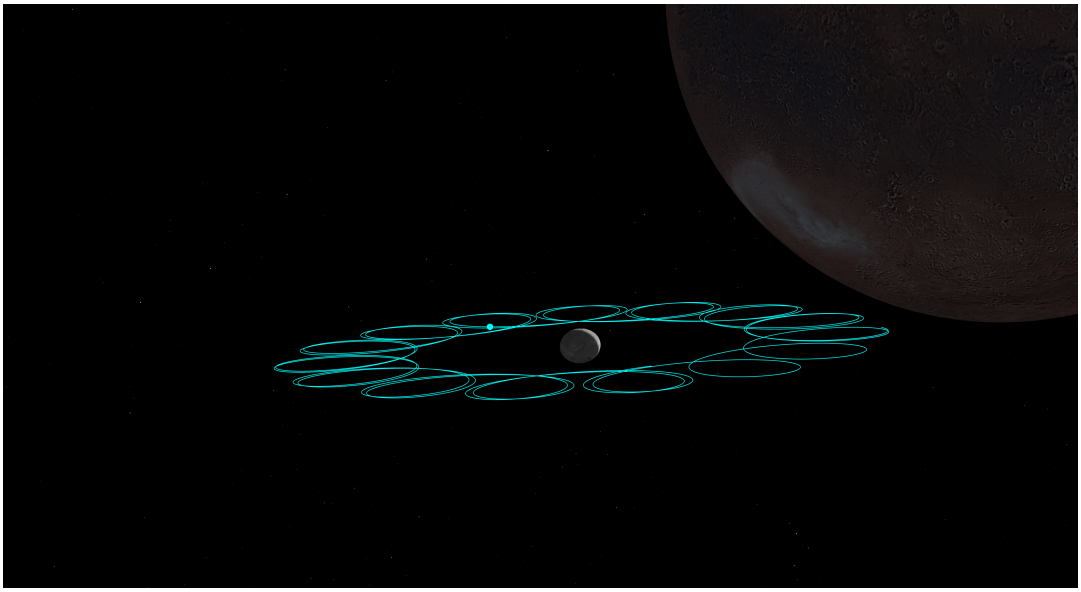

Figure 3.12. Example member of the f family as viewed in the Deimos-centered inertial frame. Mars included for spatial awareness.

3.5 Quasi-Satellite Orbits

The stability of planar DROs is a very useful property from a mission design standpoint as it allows for long-term orbits that can be maintained with little to no fuel cost and operational complexity. However, for better viewing geometry and global coverage of a body, it can be more desirable for a target science orbit to be inclined relative to the equator of the body.

When a distant retrograde orbit is given a non-zero velocity in the out of plane direction (the Z direction), they are inclined out of the XY plane in the rotating frame. These orbits are sometimes referred to as quasi-satellite orbits [16, 19, 27].

The term quasi-satellite orbit is utilized in both astrodynamics and celestial mechanics, and refers generally to the motion of a small body (or spacecraft) near a larger primary, but outside the Hill sphere of that primary [52, 53]. For example, in the Sun - Earth system, asteroid 2016 HO_3 appears to very slowly orbit the Earth with a period of about one Earth year [54]. The asteroid and the Earth both have a 1:1 ratio of their periods about the Sun. Given that 2016 HO_3 is well outside the

Earth's Hill sphere, it is more appropriate to think of it as a Sun-orbiting body that is perturbed by the Earth rather than an Earth satellite, hence *quasi*-satellite.

QSOs can be generated in many three-body systems, and were first operationally considered and utilized for the *Phobos 1* and *Phobos 2* missions [52, 55, 56]. In the case of the Mars - Deimos system, much of the f family exists outside the Hill sphere of Deimos. Given this, most of the family could be thought of as Mars-centric objects that stay in the Deimos vicinity. By the typical definitions of a quasi-satellite orbit, the members of the family that exist inside the Hill sphere (inside an X_0 value of approximately 25 km), would not apply. However, for this work, all of the analyzed trajectories will be referred to as quasi-satellite orbits. This is taking a more broad definition of a quasi-satellite orbit, but the low-altitude members of the family inside the Deimos Hill sphere are only a small subset of the analyzed trajectories.

When a member of this family is given a non-zero initial velocity in the Z direction, the motion in the XY plane stays the same, but there are additional oscillations in the Z direction. An example of this motion is shown in Figure 3.13.

Following the notation of Hénon, one of the early pioneers of this work, there are two methods for generating QSOs: type C_v with $Z_0 \neq 0, \dot{Z}_0 = 0$, and type B_v with $Z_0 = 0, \dot{Z}_0 \neq 0$ [57]. Given the periodic or quasi-periodic nature of these orbits, either method is equally valid for generating QSOs. This thesis will utilize B_v, which starts the trajectory in the XY plane and applies the out of plane velocity accordingly.

In the CRTBP, it is possible to generate perfectly periodic QSOs. The repetition period is a function of the ratio of the planar epicycle period to the period about the primary body (Mars in this case) [58]. Given this, there are set members of the family that can provide common ratios (1:2, 3:4, 3:5, etc.). These specific periodic trajectories with common repetitive cycles could be useful for mission operations, but they are not studied in detail in this thesis. This is primarily because the precise periodicity can be hard (or expensive in terms of fuel costs) to maintain once they are evaluated in the ephemeris model. Typically, once the trajectories are moved into the ephemeris model, they transition into something that is more quasi-periodic. The

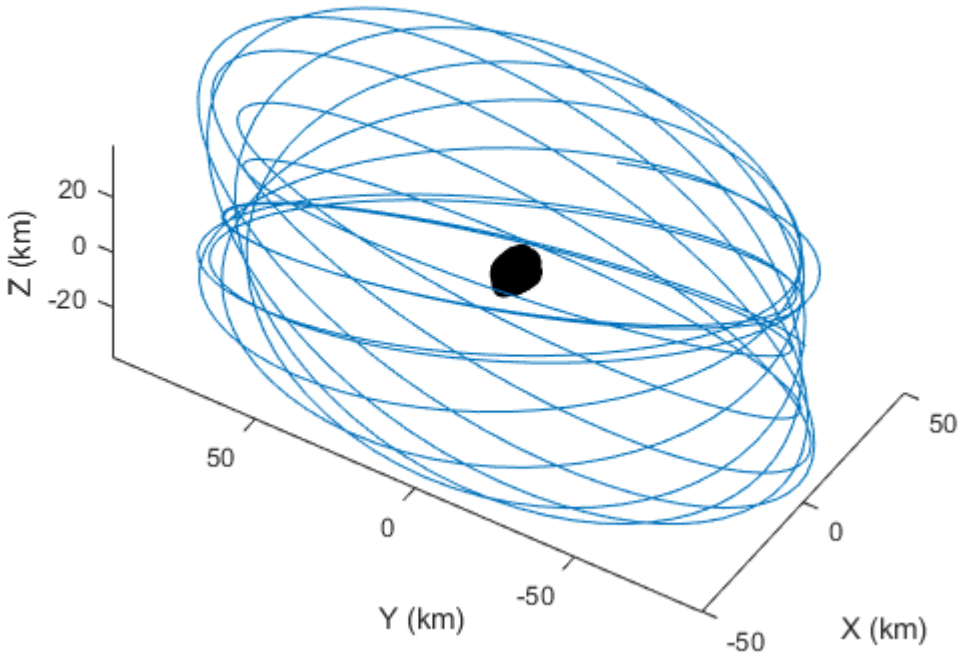

Figure 3.13. Example QSO as viewed in the Mars - Deimos rotating frame.

behavior of QSOs in the inertial frame is similar to that of DROs. A top-down and side view of this behavior is shown in Figures 3.14 and 3.15.

The motion appears complex in the inertial frame, but maintains the same basic properties as seen in the inertial motion of DROs. The only difference is the addition of the out of plane velocity.

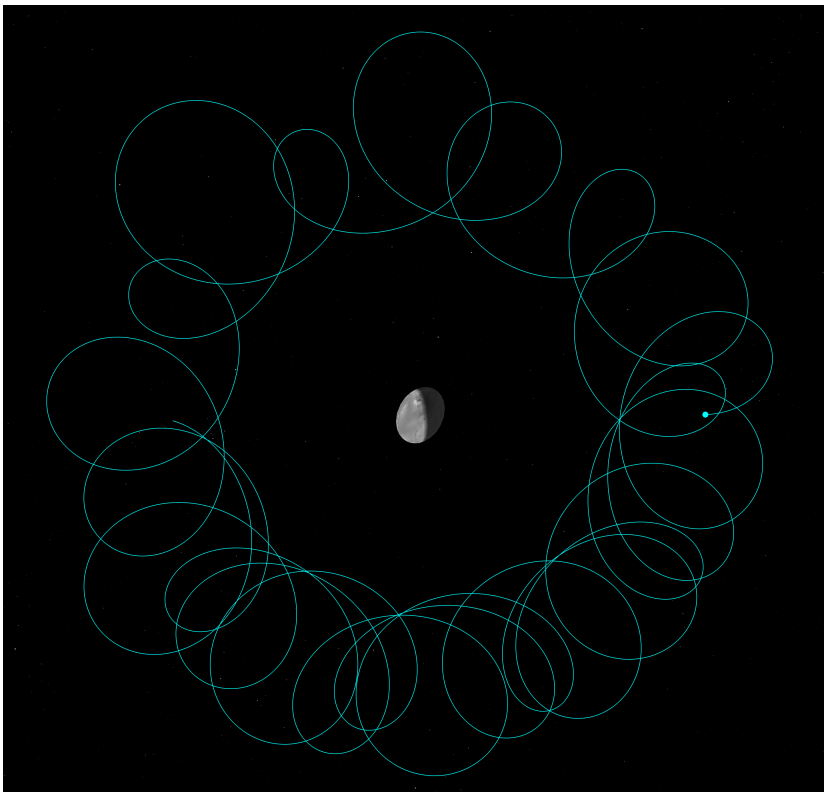

Figure 3.14. QSO as viewed in the Deimos-centered inertial frame from above.

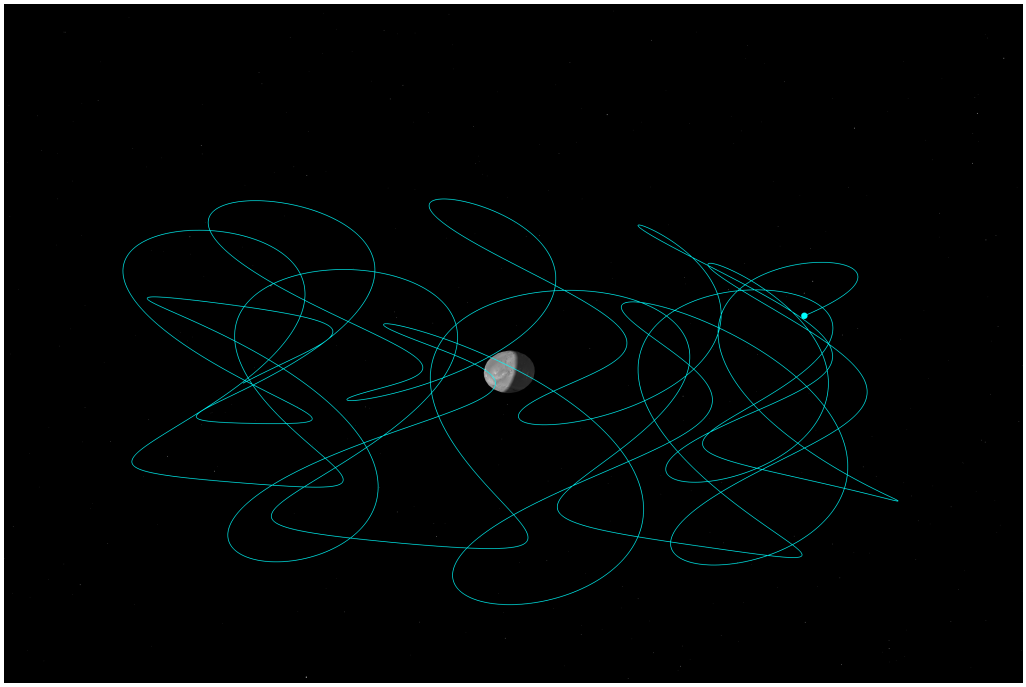

Figure 3.15. QSO as viewed in the Deimos-centered inertial frame from the Mars - Deimos orbital plane.

4. MISSION ANALYSIS AT DEIMOS

4.1 Stability of Quasi-Satellite Orbits at Deimos

While quasi-satellite orbits seem very promising for performing remote sensing observations at Deimos, the stability of these orbits is still important to consider. Some analytical and numerical studies of QSO stability at Phobos and Deimos have been performed by Gil and Schwartz [16], da Silva Pais Cabral [59], Canalias et al. [19], and Spiridonova et al. [27]. The stability analysis in this thesis is primarily numerical in nature, but provides a brief theoretical examination for the very low altitudes where general perturbations theory based on perturbations of Keplerian elements can be considered to be valid.

One stability metric of interest is the critical inclination, or the stable relative orbital inclination that is closest to a polar orbit about Deimos. An important caveat here is that the inclination is defined with respect to the inertial Deimos equatorial plane, not with respect to the rotating frame in which these QSOs are usually visualized. This definition of inclination is the standard definition for a two-body problem, but it is important to note given that many of these orbits exist well outside the point where Keplerian elements are valid.

From a coverage standpoint it is desirable to maximize the inclination with respect to Deimos in order to provide observations of the polar regions. However, as the inclination gets closer to polar, perturbations from the Martian gravitational potential can have a more destabilizing effect on the trajectory, causing the spacecraft to impact Deimos or leave the Deimos vicinity. Some instability may be tolerable for a mission that can perform frequent stationkeeping maneuvers, but this is very much mission and spacecraft-dependent. Given this balance between instability and suitability for

remote sensing observations, studying the critical inclination across members of the family provides important insights.

4.1.1 Theoretical Approach

The first approach at finding the critical inclination of QSOs about Deimos was to use general perturbations theory and averaging assumptions to find the inclination at which the eccentricity of the orbit about Deimos is unbounded. By isolating only the first-order secular terms, a set of orbital element derivatives known as the Secular Lagrange Equations can be derived. This derivation is demonstrated by Scheeres and other authors [26], and the equations are summarized in Equations 4.1 - 4.5 for the evolution of a satellite in orbit about a planetary moon.

$$\frac{da}{dt} = 0 \tag{4.1}$$

$$\frac{di}{dt} = -\frac{15}{16}\frac{N_S^2}{n}\frac{e^2}{\sqrt{1-e^2}}\sin 2i \sin 2\omega \tag{4.2}$$

$$\frac{d\Omega}{dt} = -\frac{3}{8}\frac{N_S^2}{n}\frac{\cos i}{\sqrt{1-e^2}}[2 + 3e^2 - 5e^2\cos 2\omega] \tag{4.3}$$

$$\frac{de}{dt} = \frac{15}{8}\frac{N_S^2}{n}e\sqrt{1-e^2}\sin^2 i \sin 2\omega \tag{4.4}$$

$$\frac{d\omega}{dt} = \frac{3}{8}\frac{N_S^2}{n}\frac{1}{\sqrt{1-e^2}}[5\cos^2 i - 1 + 5\sin^2 i \cos 2\omega + e^2(1 - 5\cos 2\omega)] \tag{4.5}$$

In these equations, N_S represents the mean motion of the planetary moon about its planet, and n represents the mean motion of the satellite about the moon.

These equations can be simplified based on the general assumption that the orbit of the satellite about the moon is near-circular. If the assumption is made that the eccentricity is close to zero, and any higher order eccentricity terms are approximately zero, the equations can be re-written as:

$$\frac{da}{dt} = 0 \tag{4.6}$$

$$\frac{di}{dt} = 0 \tag{4.7}$$

$$\frac{d\Omega}{dt} = -\frac{6}{8}\frac{N_S^2}{n}\cos i \tag{4.8}$$

$$\frac{de}{dt} = \frac{15}{8}\frac{N_S^2}{n}e\sin^2 i\sin 2\omega \tag{4.9}$$

$$\frac{d\omega}{dt} = \frac{3}{8}\frac{N_S^2}{n}[5\cos^2 i - 1 + 5\sin^2 i\cos 2\omega] \tag{4.10}$$

When this simplification is made, Equations 4.9 and 4.10 become coupled, and the stability characteristics of e can be observed while treating N_s and n as constants. For the resulting coupled equations, there is a range of initial inclinations that result in bounded eccentricities, or stable orbits.

For Deimos, the range of stable retrograde inclinations tends to be from approximately 140 - 180 degrees. However, the basic assumptions that are made in this approximation are only valid at very low orbital altitudes. When the f family about Deimos was explored in Section 3.4, it was shown that the family is only near-circular for very low altitudes and quickly approaches a 2:1 Y amplitude to X amplitude ratio. The assumptions involved in using general perturbations to estimate the evolution of the Keplerian elements are quickly violated, and in the numerical approach, it will be shown that the numerical stability behavior as a function of the inclination is more complicated than originally predicted via the Secular Lagrange Equations and near-Keplerian assumptions.

4.1.2 Numerical Approach

Given that the f family of orbits about Deimos (and the QSOs that bifurcate off of it) generally violate assumptions of Keplerian motion with respect to Deimos, a numerical approach was utilized in order to study the critical inclination across the f family.

Each member of the planar f family was propagated with CRTBP dynamics with a set of out of plane velocities $\dot{Z}_0 \neq 0$. Each trajectory was propagated for 30 days to determine which set of initial conditions remained within the Deimos system and which either impacted Deimos or exited the vicinity into a fully Mars-centric orbit.

For the trajectories that leave the vicinity of Deimos, the mechanism is typically that perturbations disrupt the 1:1 period ratio (with Deimos, and with respect to Mars) discussed in the introduction to QSOs in Section 3.5. Once this resonance is disrupted, the spacecraft will have a secular drift away from Deimos. The resulting stability map of initial conditions is shown in Figure 4.1.

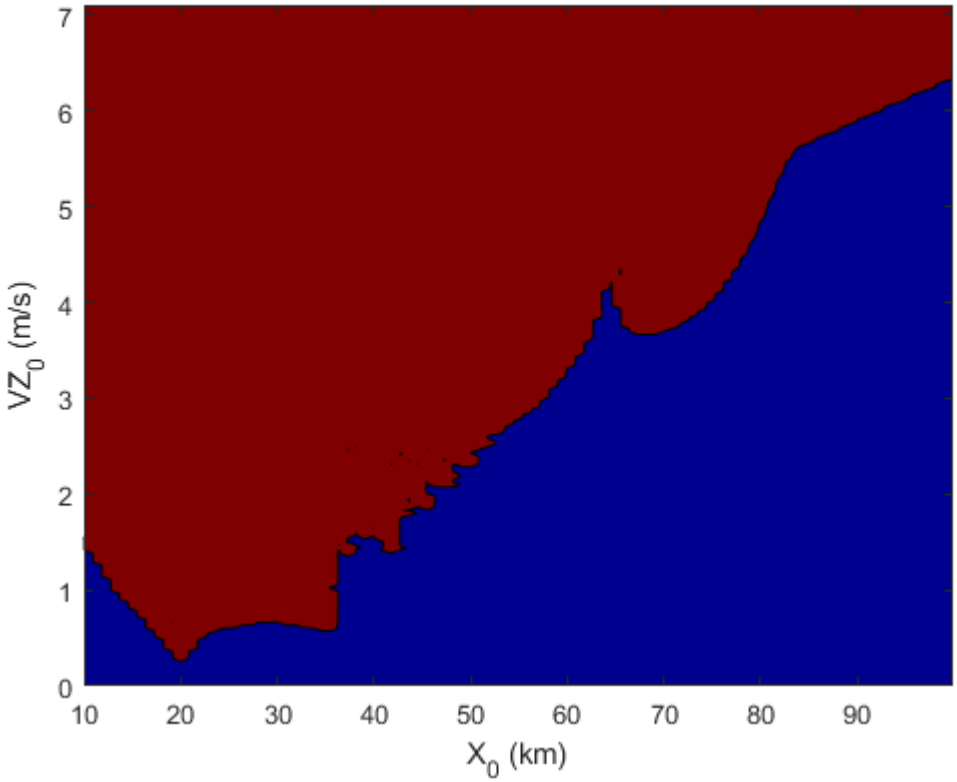

Figure 4.1. Stability map of Deimos QSOs based on CRTBP dynamics. Blue: Remains in orbit about Deimos. Red: Impacts or leaves the vicinity of Deimos.

The stability criteria here shows an interesting, but somewhat expected, trend: there is an inflection point at around $X_0 = 20$ km which corresponds to the location of the Mars - Deimos L1 and L2 points. Note the similar inflection point for initial conditions and stability indices for the planar f family. Once the family is outside of

this point, the allowable out of plane velocity continues to increase. There is a rather sharp increase at around 38 km and a small peak around 65 km.

As a whole, no member of the family that was analyzed could remain at Deimos with an initial out of plane velocity $\dot{Z}_0 > 6.5$ m/s. If the allowable out of plane velocity is taken as a sensitivity metric in and of itself, the most sensitive portion of the family (to out of plane perturbations) is at $X_0 = 20$ km.

From the stability map shown in Figure 4.1, it is possible to isolate the value of $\dot{Z}_0$ that serves as a transition between the stable and unstable region, and use that out of plane velocity to solve for the critical inclination of that member of the family. This critical inclination calculation is shown across the family in Figure 4.2.

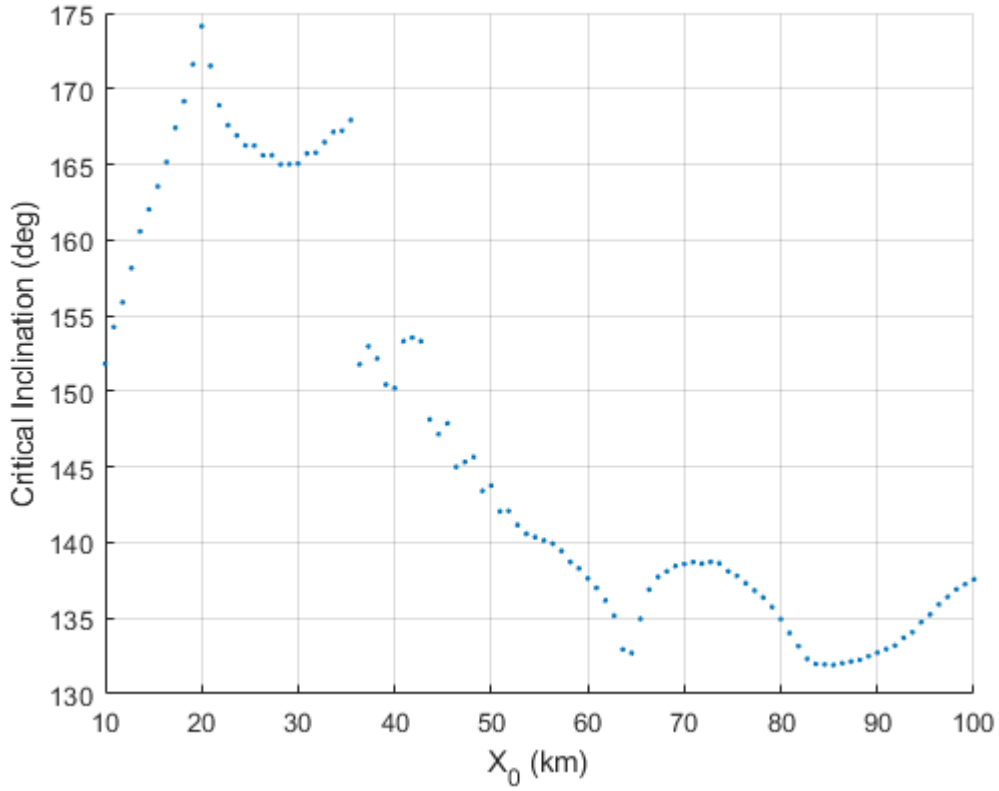

Figure 4.2. Critical inclination across the f family.

This trend in critical inclination shows the transitional nature of the f family about Deimos as it moves from a Deimos-dominated trajectory to a Deimos-perturbed trajectory to something that is hardly affected by Deimos at all.

The critical inclination for the closest members to Deimos is approximately 150 degrees. This is close to the critical inclination as predicted by the Secular Lagrange Planetary Equations and described in Section 4.1.1, but not exactly, and it very quickly diverges from this estimate.

Studies of DROs in the Earth-Moon system have shown that as the members of the family grow larger, the critical inclination tends to approach 180 degrees [60]. This is the behavior that is seen for members with $X_0 = 10 - 20$ km. However, many of these previous studies in the Earth-Moon system did not examine DROs that were very far outside of the Moon's Hill sphere. For the f family, most of the family lies well outside this region.

As the family grows past this region, and the dynamics begin to approximate unforced relative motion in the vicinity of Deimos, it was expected that the critical inclination would open back up towards polar. The Clohessy-Wiltshire equations and other unforced relative motion dynamic models allow for some relative inclination, so as the dynamics begin to approximate unforced relative motion, this is expected. This is indeed the behavior observed once the family is completely outside the Hill sphere. There is a steep drop-off at around 30 km, and the critical inclination for the family remains between 130 and 150 degrees for the rest of the analyzed members.

In relation to designing science orbits, there are three features of this critical inclination distribution that are particularly interesting. First, the rapid jump from more than 165 degrees to around 150 degrees between X_0 = 35 - 40 km. There are critical inclinations closer to polar elsewhere in the family, but this very rapid change allows for coverage of significantly higher latitudes at Deimos at relatively low altitudes. The second and third features are the local extrema located at $X_0 = 64$ km and $X_0 = 85$ km respectively. These two points represent the closest stable inclinations to polar that are possible across the analysed members of the f family,

and provide the furthest northern and southern Deimos ground tracks of any of the analyzed trajectories.

4.2 Science Orbit Design

4.2.1 Batch Search

To design a target science orbit for global, high-resolution observations of Deimos, a tool was developed that computes the coverage and spatial resolution of simulated measurements for any arbitrarily-shaped body, an ephemeris file of a trajectory about that body, the sensor parameters, and any desired solar constraints.

The purpose of the tool is to process potential science orbits in bulk to gain an understanding of the entire orbital tradespace for a given sensor. Typically the coverage of a body can only be optimized once the science requirements and sensor parameters are known, but this analysis seeks to find promising science orbits for a range of potential sensors and resolution requirements. The cases evaluated in this batch study are shown in Table 4.1.

Table 4.1. Deimos Coverage Cases Evaluated

Measurement	**Instrument**	**FOV**	**Requirement**
Thermal Infrared	FLIR Tau 2, 100mm lens	6.2 x 5.0 deg	30, 10, 5 m/px
	FLIR Tau 2, 60mm lens	10.4 x 8.3 deg	
Visual	ECAM C30, 30mm lens	12.5 x 9.4 deg	5 m/px
	ECAM C50, 12.6mm lens	25.9 x 19.4 deg	
	ECAM C50, 30mm lens	10.9 x 8.2 deg	
	ECAM C50, 63mm lens	5.2 x 3.9 deg	

The FLIR Tau 2 is a thermal camera suitable for small spacecraft, and would be a very good candidate for a NASA Small Innovative Missions for Planetary Exploration

(SIMPLEx)-class mission [1]. The instrument would require an addition of narrow-band filters in order to utilize it as a multispectral spectrometer, but this is a process that has been previously demonstrated [1]. Even the most lenient requirement of 30 m/px would provide vast improvements over current models at Deimos and would provide useful infrared maps of the surface. However, also testing higher resolutions allows for an understanding of what the highest potential resolution could be for a near-global map.

The ECAM line of visual cameras from Malin Space Science Systems has flown on multiple missions, including OSIRIS-ReX [1]. For visual observations, the only resolution requirement analyzed is 5 m/px.

The goals of the large batch analysis are to find a potential science orbit that:

1. Maximizes the percent coverage of the Deimos surface subject to basic sensor-driven constraints

2. Minimizes the spatial resolution of the measurements

These two goals are often in conflict. For example, a distant orbit will likely meet the percent coverage criteria very easily, but will only provide low-resolution measurements. Conversely, a very close orbit will provide high-resolution measurements, but may never see the entire body.

For the batch search, the output evaluated for each setup is the percent coverage of Deimos for a set of quasi-satellite orbits. In order to be counted as a "successful" observation, it must be within the field of view of the sensor, must meet the resolution requirement, and must meet additional solar constraints.

The batch search is performed via the following procedures:

- The set of initial conditions for the evaluated QSOs span $X_0 = 10 - 100$ km, and $\dot{Z}_0 = 0 - 10$ m/s.

- All initial conditions are propagated for 14 days in the ephemeris model using the force model described in Section 2.5.

- Measurements made in the visual band are constrained to be only on sunlit geometry.

The evaluated duration of 14 days represents the time period between ground-commanded maneuvers that can be used to maintain the desired orbit. As seen in Section 4.1, some of the evaluated orbits are unstable and *will* escape the Deimos vicinity. However, they are still included in this analysis in order to gain a full view of the orbital tradespace.

Another important note is that 14 days is significantly shorter than a typical science phase of a mission, but this batch search is not meant to be a fully mature coverage analysis, it is meant to narrow the orbital tradespace in order to perform a higher fidelity study with mission-specific constraints. The observation geometry repeats over time, so by cutting off this analysis at 14 days, there is no coverage information that is lost for basic coverage alone. For more complex solar constraints that have long-period trends, there is information lost, but these constraints will be evaluated with a higher fidelity long-term coverage analysis in Section 4.2.2.

The output from this batch search is a "map" of the percent coverage of the Deimos surface that meets the specified spatial resolution requirements (and any additional constraints) for the full set of initial conditions evaluated.

The set of initial conditions are propagated without any regard to the stability behavior examined in Section 4.1.2. What this means is that some of the trajectories evaluated do leave the vicinity of Deimos. These are primarily the initial conditions with very high values of $\dot{Z}_0$, but to assist in interpreting the coverage maps, the stability boundary determined in Section 4.1.2 is overlaid on top of the maps.

Thermal Infrared Measurements: 5 m/px requirement

The coverage maps of thermal infrared measurements at 5 m/px are shown in Figures 4.3 and 4.4.

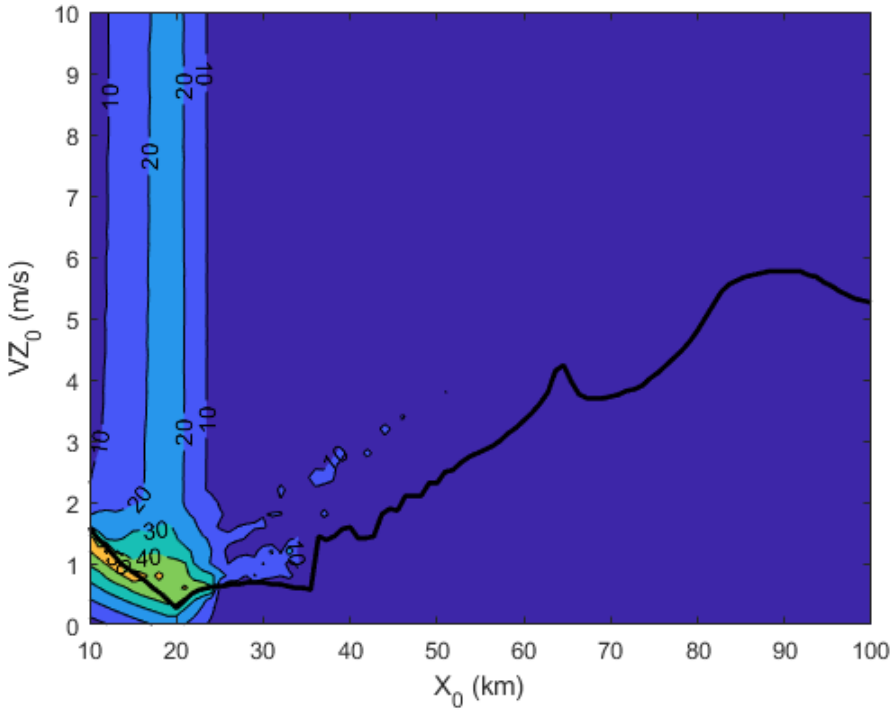

Figure 4.3. Percent coverage for thermal infrared measurements at 5 m/px using the FLIR Tau 2 60mm lens.

These coverage maps show that for this particular combination of evaluated sensors and resolution requirements, there are no QSOs in the evaluated set that come close to providing global coverage at Deimos.

Keep in mind however that these science requirements and sensors are notional in nature. For applying this batch method to a mission in development, this realization would most likely warrant the analysis of a new, more capable sensor if the science team wanted to support measurements at 5 m/px.

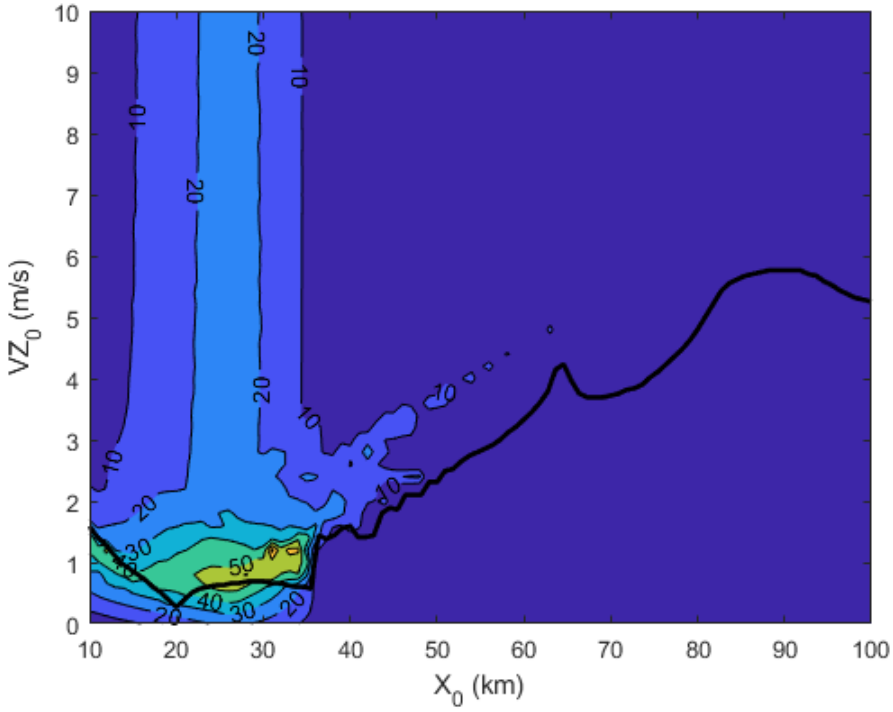

Figure 4.4. Percent coverage for thermal infrared measurements at 5 m/px using the FLIR Tau 2 100mm lens.

Thermal Infrared Measurements: 10 m/px requirement

The coverage maps of thermal infrared measurements at 10 m/px are shown in Figures 4.5 and 4.6.

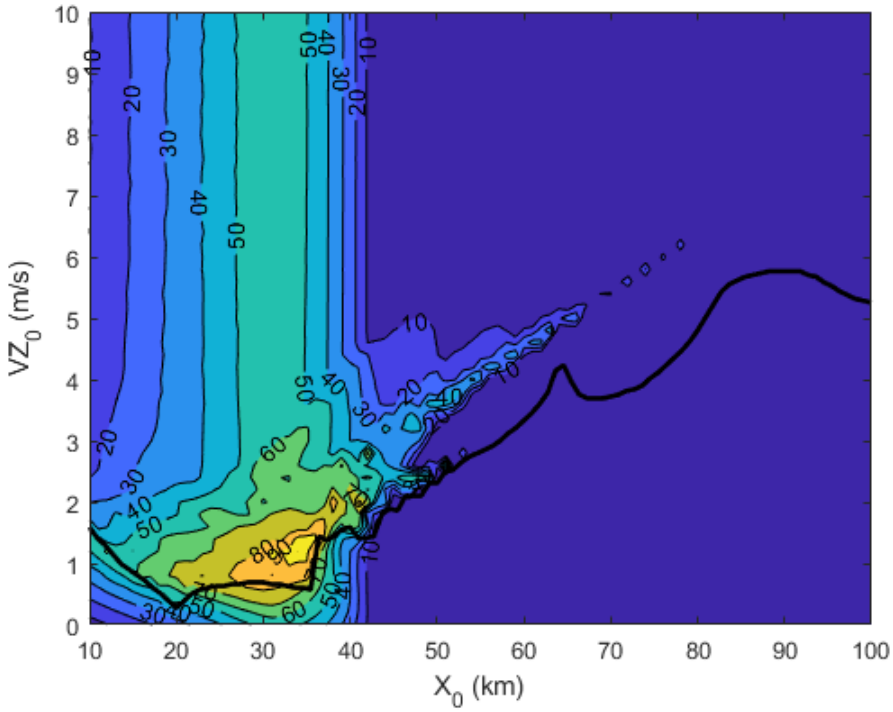

Figure 4.5. Percent coverage for thermal infrared measurements at 10 m/px using the FLIR Tau 2 60mm lens.

These coverage maps are much more interesting than the 5 m/px case because they demonstrate the trade-offs between coverage, altitude, and out of plane motion.

For both the 60mm and 100mm lenses, the percent coverage of Deimos at 10 m/px is maximized at an intermediate range - far enough away to provide near-global visibility of the body, but not so far that spatial resolution of the measurements is degraded below the requirement.

For this notional set of science requirements and evaluated sensors, the 60mm lens can provide greater than 90% coverage in one small portion of the tradespace,

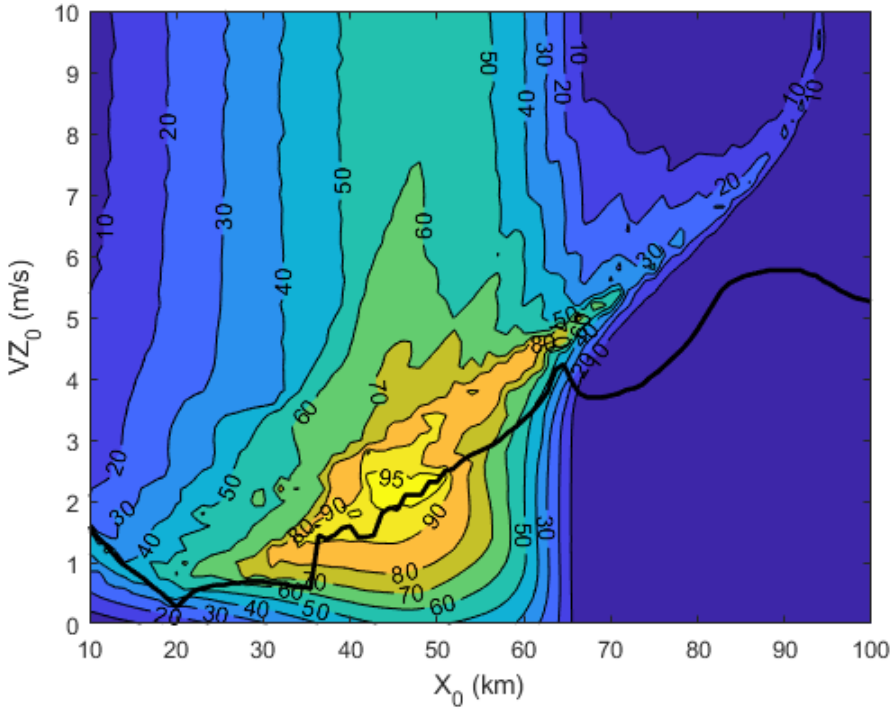

Figure 4.6. Percent coverage for thermal infrared measurements at 10 m/px using the FLIR Tau 2 100mm lens.

while the 100mm lens and its more narrow field of view can provide greater than 95% coverage in a portion that exists further away from Deimos.

An interesting observation for these two maps is that the region that maximizes the coverage with both lenses lies slightly outside the stable region. This is somewhat to be expected given that the unstable regions are the regions where the out of plane motion is greater, allowing for better observations of the Deimos polar regions.

It is also important to remember that the boundary between unstable and stable is not necessarily a hard boundary where operations cannot exist. The analysis that originally generated the stability boundary used a 30 day propagation period, meaning that at some point within that 30 days, the trajectories in the unstable region of the tradespace impacted Deimos or escaped the Deimos vicinity. For trajectories that are very close to the boundary, it is very likely that these orbits could be maintained with a minimal stationkeeping cadence on the order of one burn per week (or less) without leaving the Deimos vicinity. Spacecraft have operated at the Sun - Earth L1 and L2 points for decades, and all of these orbits are mathematically unstable. Whether a spacecraft can maintain orbits slightly into the unstable regime as determined by the previous numerical study is a question of how far into the unstable region they are, the spacecraft fuel capacity, and the mission navigation capability.

Thermal Infrared Measurements: 30 m/px requirement

The coverage maps of thermal infrared measurements at 30 m/px are shown in Figures 4.7 and 4.8.

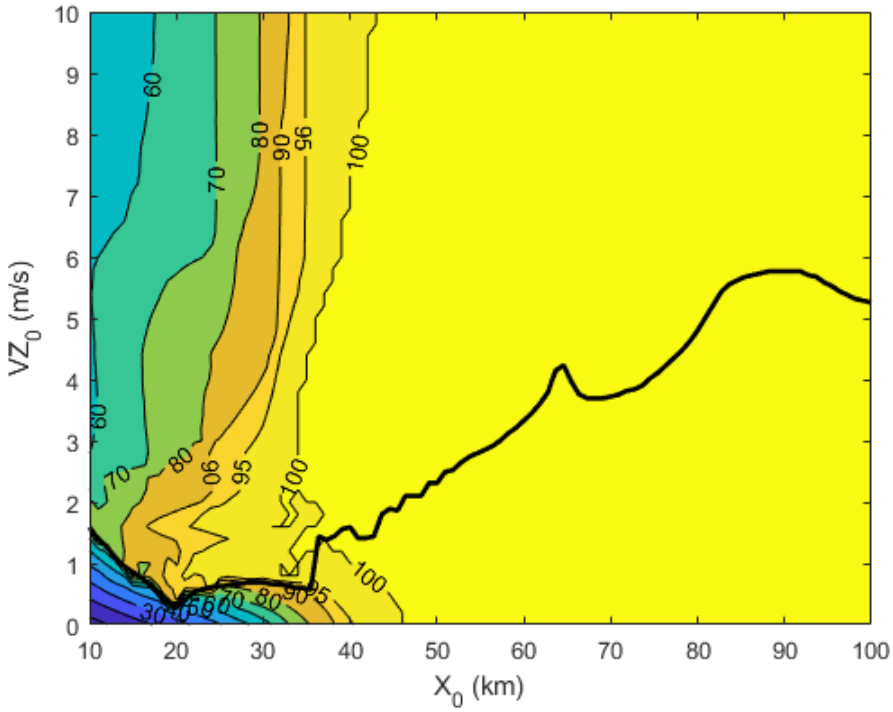

Figure 4.7. Percent coverage for thermal infrared measurements at 30 m/px using the FLIR Tau 2 60mm lens.

These two coverage maps show that with both lenses, 30 m/px is a very achievable science requirement at a wide range of trajectories. In fact, truly global coverage is obtainable with equatorial orbits assuming that the altitude is high enough.

If the science requirement for thermal infrared observations was set at 30 m/px, placing a spacecraft into a equatorial, planar DRO could be a very promising approach for a low-cost mission. Equatorial DROs are extremely stable and could reduce the onboard fuel requirements and operational complexity of a mission.

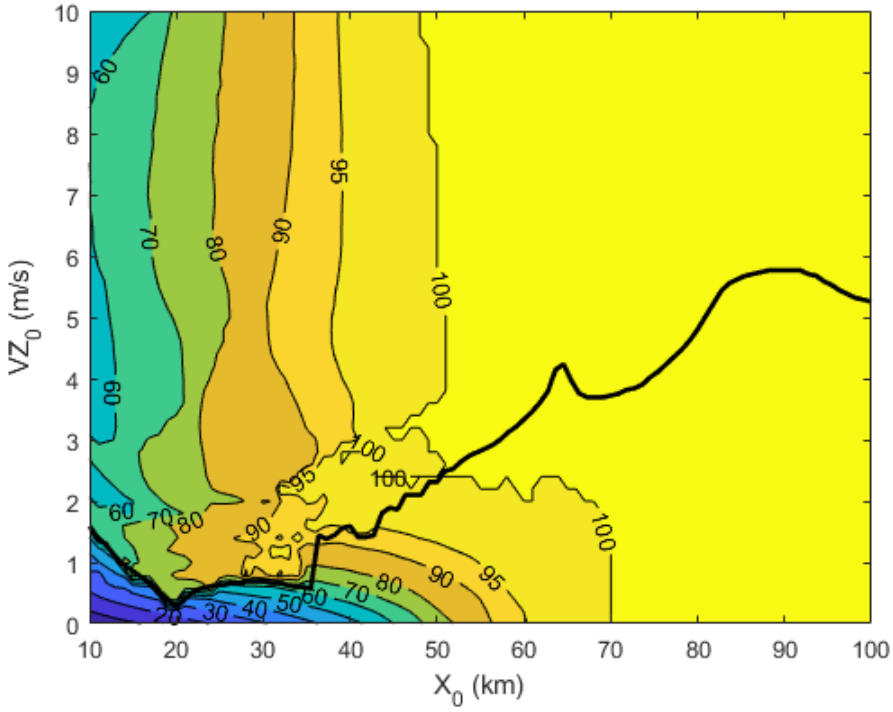

Figure 4.8. Percent coverage for thermal infrared measurements at 30 m/px using the FLIR Tau 2 100mm lens.

Visual Measurements: 5 m/px requirement

Next, we can evaluate all four sensor/lens combinations for the visual measurements. The coverage maps of visual measurements at 5 m/px are shown in Figures 4.9, 4.10, 4.11, and 4.12.

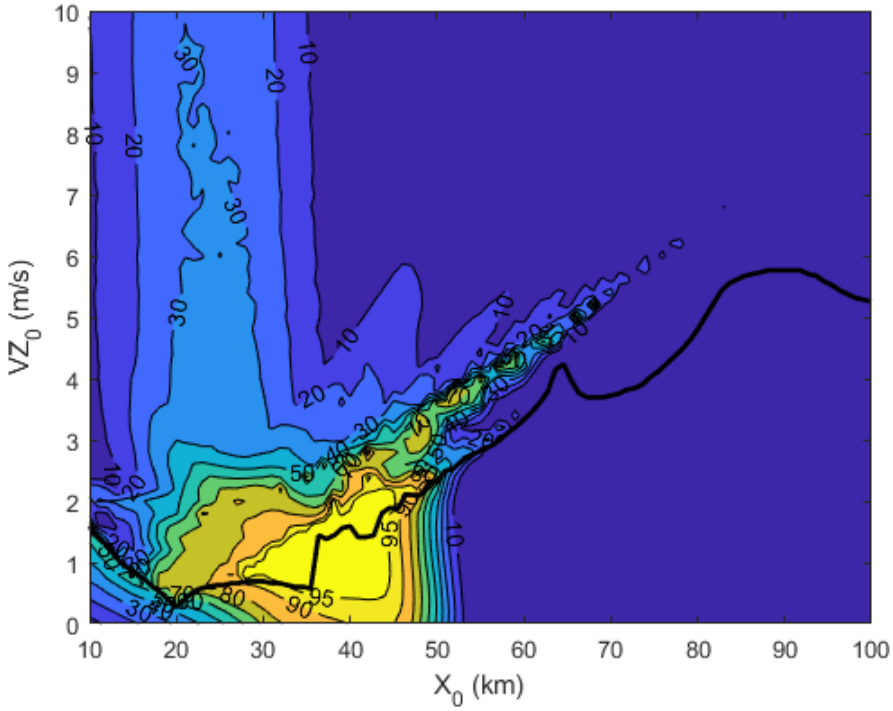

Figure 4.9. Percent coverage for visual measurements at 5 m/px using the ECAM C30 30mm lens.

This analysis shows that a global mapping of Deimos via visual observations can be performed at 5 m/px or less with any of the four sensor/lens combinations.

Additionally, for the ECAM C50 with both a 12.6mm and 30 mm lens, it is possible to generate a near-global map with observations from an equatorial orbit alone. As discussed previously, this could be very useful, particularly for a small satellite mission to Deimos.

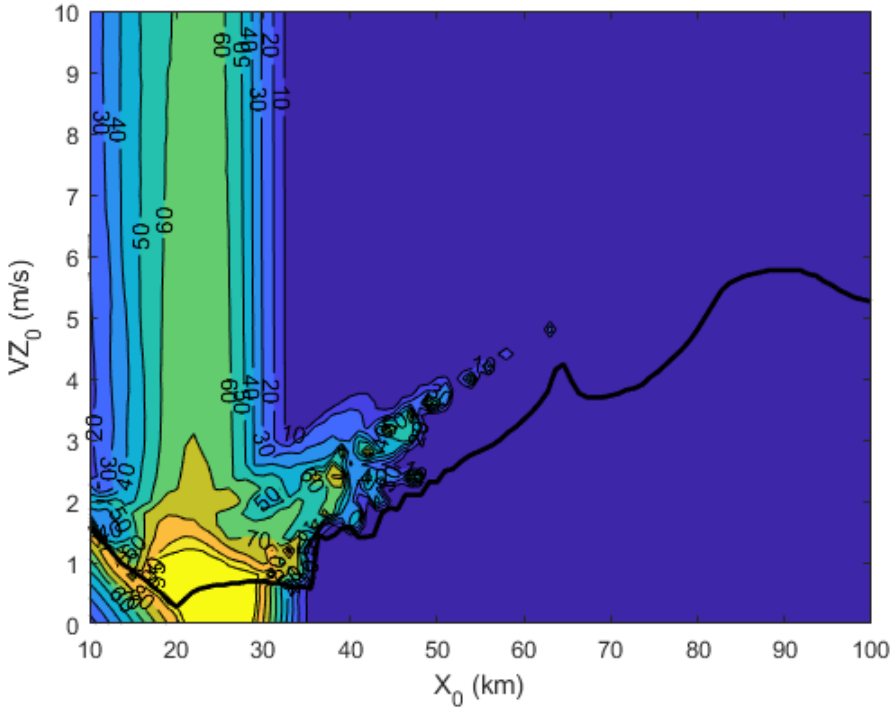

Figure 4.10. Percent coverage for visual measurements at 5 m/px using the ECAM C50 12.6mm lens.

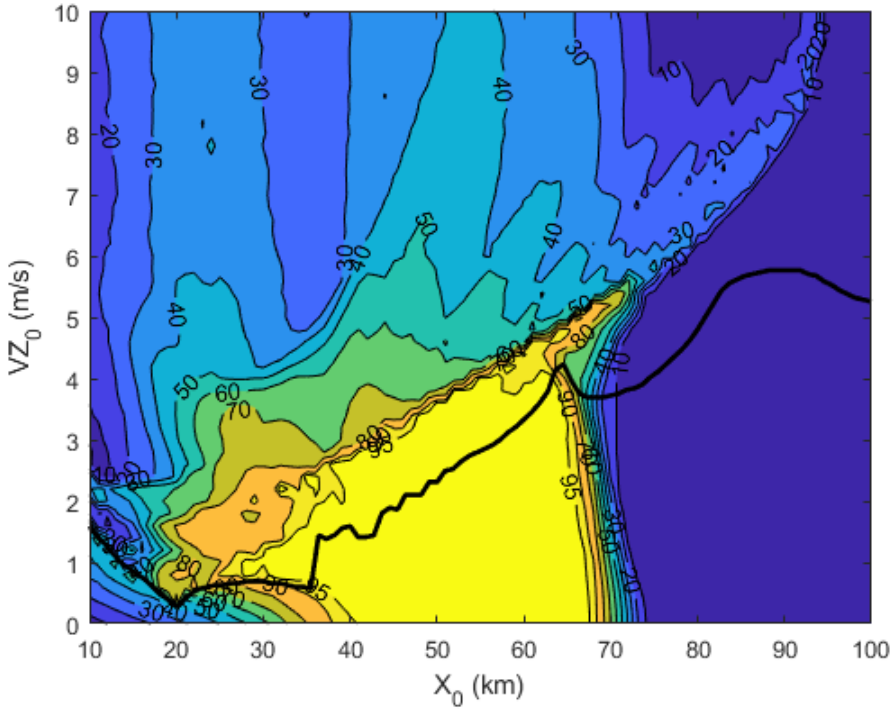

Figure 4.11. Percent coverage for visual measurements at 5 m/px using the ECAM C50 30mm lens.

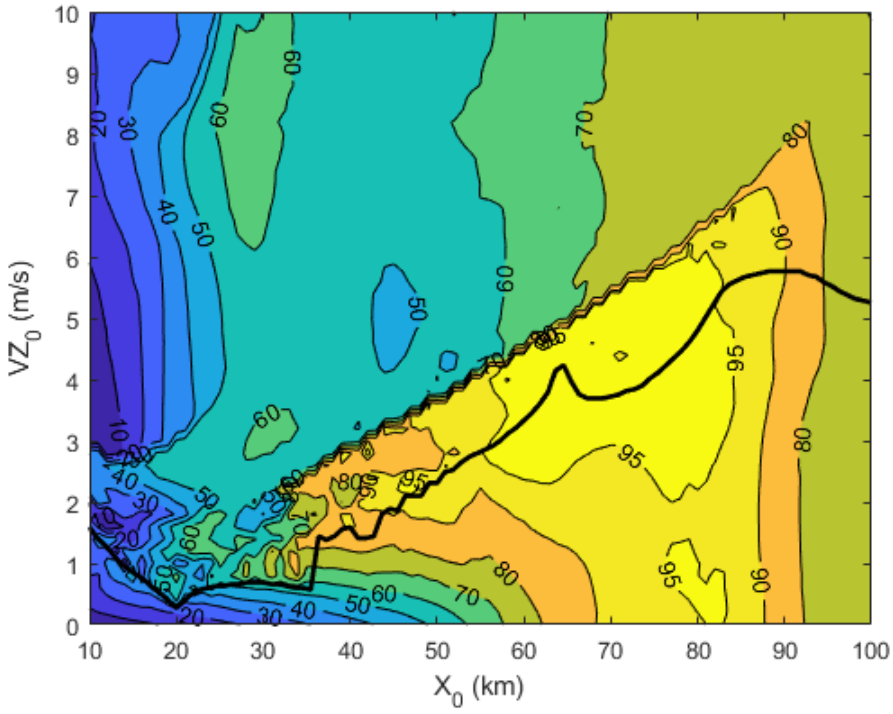

Figure 4.12. Percent coverage for visual measurements at 5 m/px using the ECAM C50 63mm lens.

4.2.2 Long-Term Coverage Analysis of Selected QSOs

To perform long-term coverage analyses that take into account more complex solar constraints that may have long-term periodic trends, a subset of the previously analyzed QSOs are generated over 6 months, starting on October 1, 2025. For this analysis, the number of analyzed sensors and resolution requirements was decreased to just one sensor and one resolution requirement for both the thermal infrared and visual band analysis.

For the long-term analysis, the two selected sensors and requirements were the FLIR Tau 2 with a 100mm lens to take thermal infrared measurements at 10 m/px, and the ECAM C50 with a 30mm lens in order to take visual measurements at 5 m/px. These two instruments are summarized in Table 4.2.

Table 4.2. Deimos Long-Term Coverage Cases Evaluated

Measurement	**Instrument**	**FOV**	**Requirement**
Thermal Infrared	FLIR Tau 2, 100mm lens	6.2 x 5.0 deg	10 m/px
Visual	ECAM C50, 30mm lens	10.9 x 8.2 deg	5 m/px

The reason that these two sensors/resolutions are chosen for further analysis is because they are both capable of global or near-global coverage with the more simple short-term coverage analysis performed earlier, and, more importantly, the region of the orbital tradespace that provides the maximized coverage is similar for both the thermal infrared and visual sensors.

The selected FLIR Tau 2 at 10 m/px could achieve near global coverage in a relatively narrow region of the tradespace from $X_0 = 40 - 50$ km and $\dot{Z}_0 = 1.5 - 2.5$ m/s. The ECAM C50 with the selected lens can meet the coverage requirements across a wide range of the orbital tradespace from $X_0 = 40 - 65$ km. By selecting two sensors with overlapping optimal regions, it allows for the design and study of a trajectory that meets the science requirements for multiple instruments simultaneously.

The four more complex coverage cases analyzed are the following:

- **VHI: Visual, High Incidence:** Visual measurements at 5 m/px at a high incidence angle. Measurements are constrained to be on sunlit geometry at a solar elevation angle of less than 45 degrees.
- **VLI: Visual, Low Incidence:** Visual measurements at 5 m/px at a low incidence angle. Measurements are constrained to be on sunlit geometry at a solar elevation angle of greater than 45 degrees.
- **TIRL: Thermal Infrared, Lit:** Thermal infrared measurements at 10 m/px on sunlit geometry.
- **TIRS: Thermal Infrared, Shadow:** Thermal infrared measurements at 10 m/px on shadowed geometry.

For these cases, incidence angle utilizes the convention where it is defined with respect to the local normal. Using this convention, the solar incidence and solar elevation angles always sum to 90 degrees.

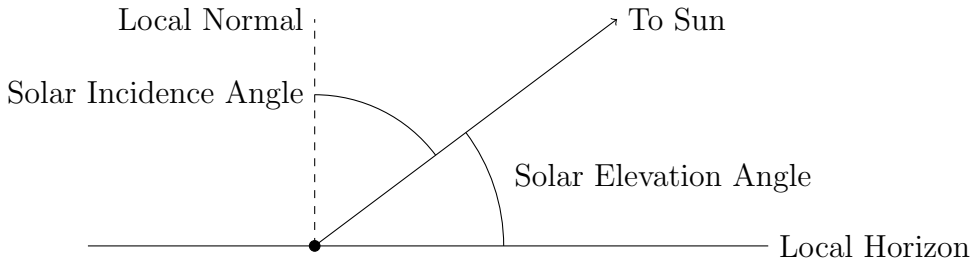

Figure 4.13. Solar incidence and elevation angle conventions.

These four cases are based on the science requirements developed for the *Chariot* PSDS3 report in 2018 [1]. For visual measurements, performing observations at a high incidence angle ensures that there are shadows on the surface and assists in the identification of topology and surface morphology. The addition of low incidence angle visual measurements are useful in correlating visual imagery with measurements

in other bands. Gathering thermal infrared properties on both sunlit and shadowed geometry assists in ascertaining thermal properties of the surface.

In order to search for potentially optimal science orbits for all desired measurements, a selection of previously-analyzed initial conditions between $X_0 = 40 - 50$ km and $\dot{Z}_0 = 1 - 2.6$ m/s was selected for a longer-term analysis. This is the general region of the tradespace that provided global or near-global coverage for both types of desired measurements with the selected sensors.

The translation between the initial out of plane velocity $\dot{Z}_0$ and an inclination with respect to Deimos is not immediately obvious and varies across the f family, so a mapping between the QSO initial conditions and the resulting inclinations with respect to Deimos is included in Figure 4.14. The region of the tradespace selected for further analysis corresponds to an inclination range of approximately 145 - 160 degrees.

In order to generate these long-term trajectories, adding in a very notional maneuver strategy is required. This strategy is not necessarily meant to mimic how the spacecraft would actually operate, it is meant to maintain the trajectory over long periods of time. Stationkeeping strategies for operations in QSOs is an ongoing area of study for researchers [19].

The maneuver strategy for maintaining these orbits takes its origins from the basic dynamics of periodic orbits in the CRTBP. In this system, the dynamics are mirrored across the X-axis, so often times targeters for periodic orbits will be programmed to target a perpendicular X-axis crossing. The strategy for this targeter is similar. For each orbit about Deimos, there is a maneuver placed at the positive X-axis crossing. This maneuver targets the state at the *next* positive X-axis crossing. For the values of the state at the next positive X-axis crossing, the targeter designs a maneuver that will yield:

1. A value X equal to the original X_0 for the QSO.

2. A perpendicular X-axis crossing such that $\dot{X}_0 = 0$.

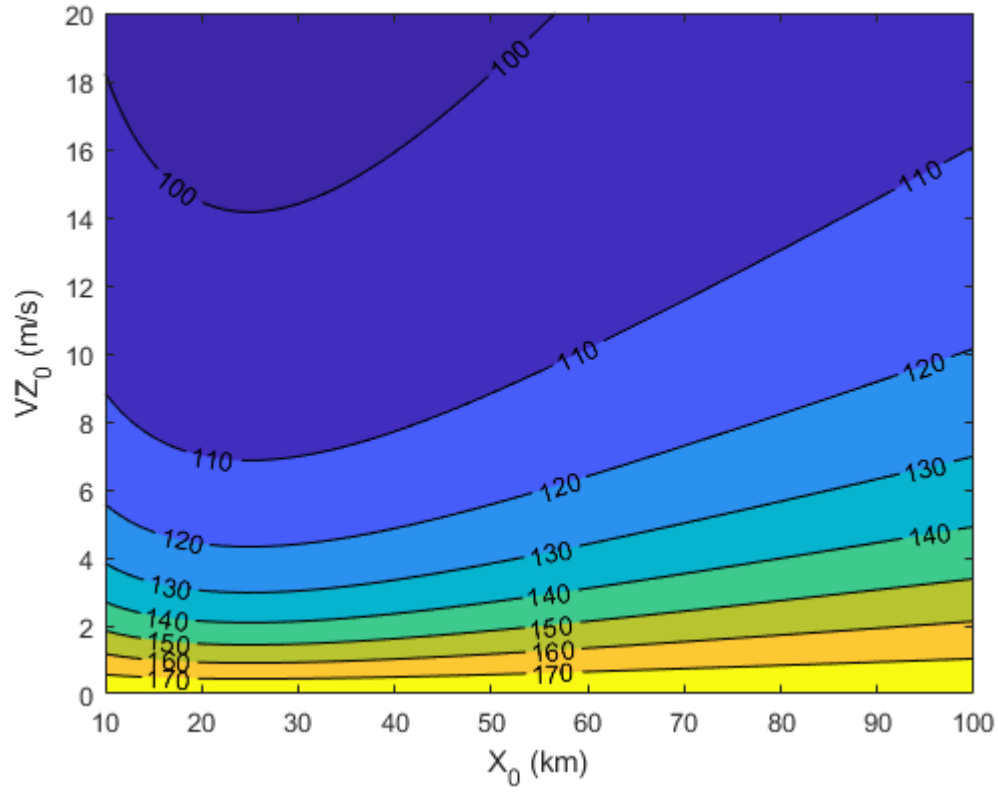

Figure 4.14. Mapping between QSO initial conditions and inclination with respect to Deimos.

A visual representation of this targeter is shown in Figure 4.15.

This targeting strategy is useful for generating long-term reference trajectories, but is not necessarily meant to perfectly mimic a stationkeeping strategy. A maneuver every orbit about Deimos would mean a maneuver nearly every day, and for some members of the family, a maneuver multiple times per day. This is likely operationally infeasible, but it yields a long-term trajectory that would be very similar to one achieved with an operational stationkeeping strategy.

A note on this strategy is that the out of plane motion is not taken into account. The targeter designs maneuvers that yield $\dot{X} = 0$ at the next X-axis crossing without regard to the values of Z or $\dot{Z}$ at that point. This is generally valid as the XY planar projection of a QSO in the CRTBP is still a periodic DRO. However, an operational

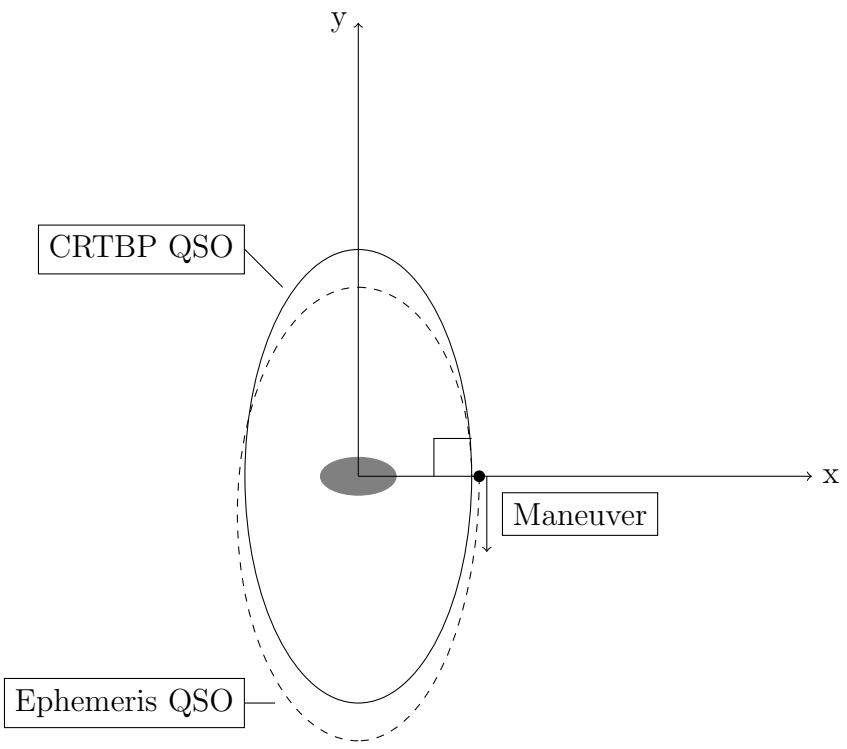

Figure 4.15. Maneuver strategy for maintaining long-term QSOs.

stationkeeping strategy might attempt to maintain the same original amplitude in the Z-axis if it drifted over time.

The percent coverage for each analyzed QSO and each analyzed measurement and constraint set is given in Table 4.3. For the two thermal infrared measurement cases, the QSO that provides the best coverage is listed in bold. This is not done for the visual measurements because the coverage is generally similar across the analyzed QSOs.

Table 4.3.: Long-Term Coverage Analysis

QSO		**Percent Coverage**			
X_0 **(km)**	$\dot{Z}_0$ **(m/s)**	**VHI**	**VLI**	**TIRL**	**TIRS**
40	1.0	99.98	90.86	78.59	79.58
40	1.2	100	90.87	82.35	83.24

Table 4.3 Continued

QSO		**Percent Coverage**			
X_0 **(km)**	$\dot{Z}_0$ **(m/s)**	**VHI**	**VLI**	**TIRL**	**TIRS**
40	1.4	100	90.96	83.82	85.56
40	1.6	100	90.00	96.39	96.05
40	1.8	100	90.97	**96.62**	**96.35**
41	1.0	100	90.96	79.07	80.12
41	1.2	100	91.08	82.53	83.89
41	1.4	100	91.08	83.26	86.04
41	1.6	100	91.09	86.01	89.20
41	1.8	100	91.10	88.22	92.20
42	1.0	100	91.02	79.10	80.51
42	1.2	100	91.06	82.08	83.91
42	1.4	100	91.05	84.64	87.22
42	1.6	100	91.07	87.07	89.93
43	1.0	100	91.02	79.81	81.01
43	1.2	100	91.05	83.28	84.82
43	1.4	100	91.04	85.31	88.12
43	1.6	100	91.03	88.55	91.07
43	1.8	100	91.06	87.88	90.37
43	2.0	100	90.99	94.84	95.26
44	1.0	100	91.00	79.82	81.02
44	1.2	100	90.99	83.50	85.32
44	1.4	100	91.04	86.16	88.01
44	1.6	100	91.03	86.85	89.50
44	1.8	100	91.01	88.15	90.73
44	2.0	100	91.02	94.31	94.22

Table 4.3 Continued

QSO		**Percent Coverage**			
X_0 **(km)**	$\dot{Z}_0$ **(m/s)**	**VHI**	**VLI**	**TIRL**	**TIRS**
45	1.0	100	90.96	80.69	81.48
45	1.2	100	91.03	83.66	85.05
45	1.4	100	91.02	85.33	87.79
45	1.6	100	90.99	86.89	89.44
45	1.8	100	91.04	87.65	89.96
45	2.0	100	91.01	87.83	90.77
45	2.2	100	91.05	91.07	93.42
45	2.4	100	91.02	93.73	95.23
45	2.6	100	91.00	92.99	94.79
46	1.0	100	91.01	80.32	81.24
46	1.2	100	91.06	82.92	84.52
46	1.4	100	91.02	85.02	87.09
46	1.6	100	90.96	86.88	89.06
46	1.8	100	90.98	89.81	91.44
46	2.0	100	91.03	87.98	90.91
46	2.2	100	91.02	90.43	92.78
46	2.4	100	91.03	90.91	93.64
46	2.6	100	90.98	92.58	94.92
47	1.0	100	91.03	79.98	80.87
47	1.2	100	90.98	82.26	83.72
47	1.4	100	91.01	83.96	86.40
47	1.6	100	91.05	85.46	87.88
47	1.8	100	91.02	85.28	88.74
47	2.0	100	91.05	87.21	89.51

Table 4.3 Continued

QSO		**Percent Coverage**			
X_0 **(km)**	$\dot{Z}_0$ **(m/s)**	**VHI**	**VLI**	**TIRL**	**TIRS**
47	2.2	100	91.03	87.61	90.41
47	2.4	100	90.98	90.62	93.30
47	2.6	100	91.03	88.48	90.61
48	1.0	100	91.03	78.86	79.60
48	1.2	100	91.03	81.03	82.86
48	1.4	100	91.04	83.42	85.62
48	1.6	100	90.99	84.14	86.53
48	1.8	100	90.97	85.40	87.83
48	2.0	100	91.01	85.78	88.68
48	2.2	100	91.01	87.18	89.54
48	2.4	100	91.02	86.80	89.62
48	2.6	100	90.97	87.28	89.66
49	1.0	100	91.04	78.00	79.38
49	1.2	100	91.03	79.76	81.99
49	1.4	100	91.02	80.84	84.00
49	1.6	100	91.00	83.05	85.56
49	1.8	100	90.99	83.99	86.81
49	2.0	100	90.99	84.35	87.13
49	2.2	100	91.02	85.28	88.53
49	2.4	100	91.01	85.40	88.84
49	2.6	100	90.94	85.99	89.09
50	1.0	100	91.05	75.35	77.79
50	1.2	100	91.03	78.09	80.57
50	1.4	100	91.00	79.87	82.67

Table 4.3 Continued

QSO		**Percent Coverage**			
X_0 **(km)**	$\dot{Z}_0$ **(m/s)**	**VHI**	**VLI**	**TIRL**	**TIRS**
50	1.6	100	91.01	81.48	84.17
50	1.8	100	90.97	82.65	85.12
50	2.0	100	90.99	83.55	86.37
50	2.2	100	90.97	83.37	86.88
50	2.4	100	90.95	82.95	87.32
50	2.6	100	90.90	83.94	87.30

Based on these long-term coverage analyses, any of the analyzed QSOs can easily provide near-global coverage with the two visual measurement cases. At a high incidence angle, truly global coverage is achievable. At a low incidence angle, coverage of over 90 percent is possible, and the remaining ten percent is due to the solar geometry, not necessarily a poor orbit design. There are some portions of Deimos near the poles where the solar elevation angle simply never reaches above 45 degrees during this analysis period, meaning that a low incidence angle measurement on that geometry is never possible.

For the thermal infrared measurements, there is more of a difference between the analyzed QSOs because 10 m/px is a more stressing requirement. The analyzed case that had the highest percent coverage is shown in Figure 4.16. This QSO can be described by the parameters $X_0 = 40$ km, $\dot{Z}_0 = 1.8$ m/s.

For all four measurement cases, this trajectory can provide greater than 90 percent coverage of the Deimos surface at the necessary coverage requirements. For the equatorial regions, particularly the regions that protrude along the Mars - Deimos radial vector, the achieved resolution can be significantly higher (higher resolution meaning lower value of m/px) than the requirement.

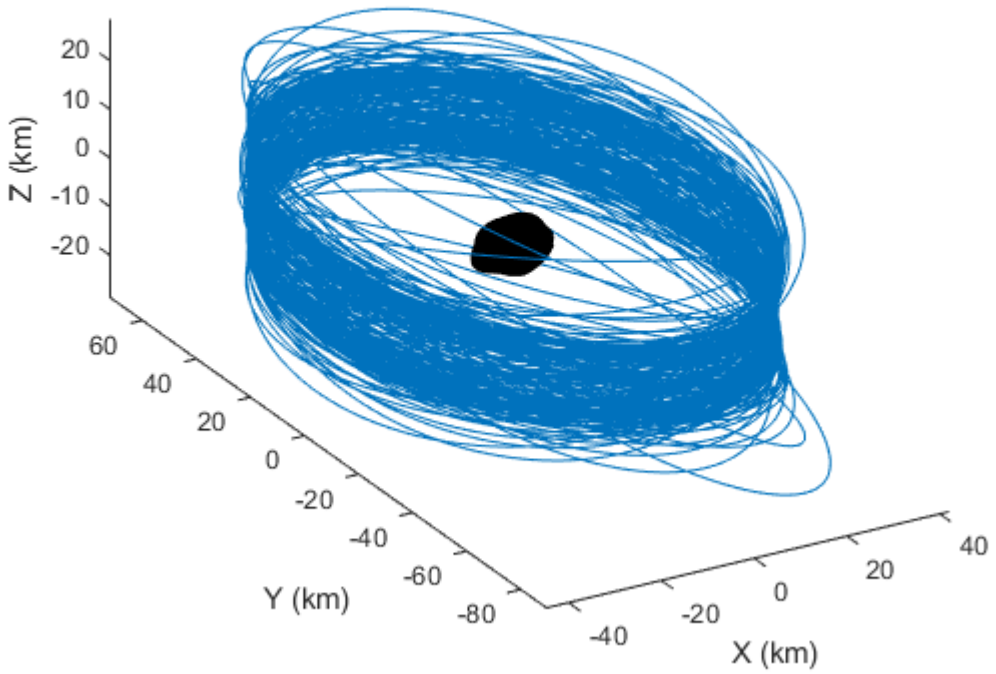

Figure 4.16. Selected QSO that maximizes coverage for analyzed cases.

The polar regions, and specifically the northern polar regions are the most stressing geometry on Deimos for observation. In fact, if the observed geometry for the thermal infrared sunlit case is examined, a small region near the northern pole is the only region that does not meet the requirements, making up the missing 3 percent of the surface that is not covered.

For the *DePhine* mission, the current mission design baseline involves leaving the standard QSO about Deimos to perform very close flybys over the poles via an unstable trajectory and then returning to the QSO [15]. These polar flybys allow for measurements of both the north and south poles of Deimos at very high resolutions. This is a very interesting mitigation for the polar coverage challenges of the more stable QSOs. They are not examined in this analysis, but could certainly be further

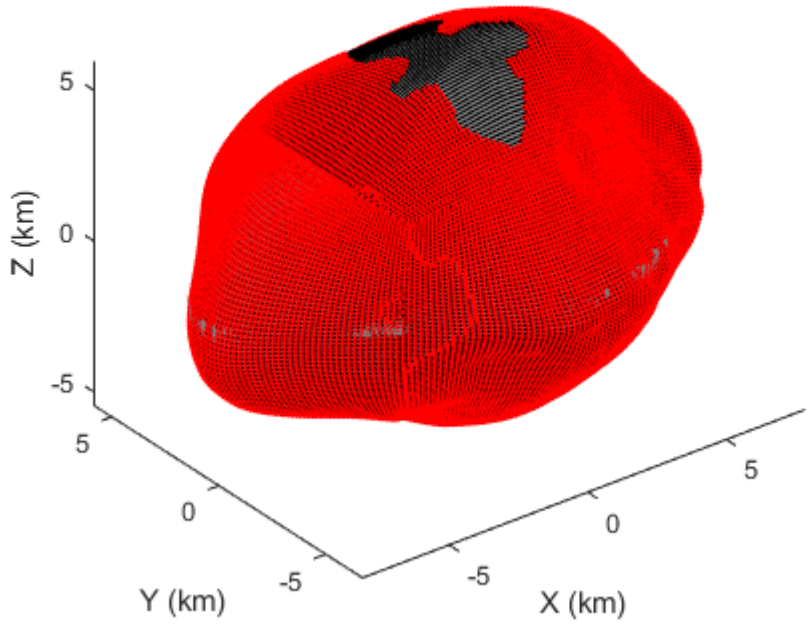

Figure 4.17. Surface coverage of Deimos for the Thermal Infrared Sunlit case.

examined in the future. If utilized, the ideal QSO for nominal operations at Deimos could likely be closer to an equatorial retrograde orbit, leaving polar observations for the flyby maneuvers described here.

4.3 Deimos Lighting Conditions

Given that all four of the higher fidelity coverage analyses incorporated solar constraints of some sort, it is important to understand the lighting environment at Deimos, specifically during the 6 month analysis period of October 2025 - March 2026.

The solar geometry at Deimos is periodic with both short-term and long-term frequencies. The short period trends are driven by the rotation of Deimos, or the

Deimos day. The longer period trends are driven by the inclination of Mars about the Sun, or Martian seasons. During different portions of the Martian orbit, the resulting solar geometry at Deimos changes.

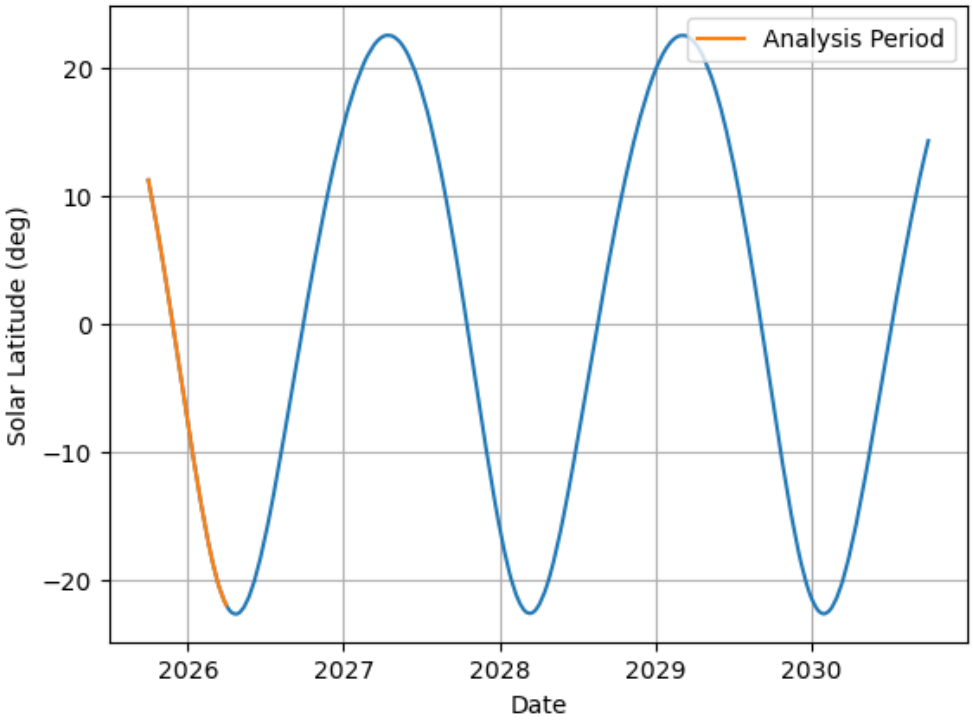

Figure 4.18. Solar latitude at Deimos over a period of 5 years.

The solar latitude at Deimos over a period of 5 years, starting at October 1, 2025, is shown in Figure 4.18. The 6 month analysis period is highlighted. This shows an approximately two year periodic trend in the latitude of the Sun as seen from Deimos. This coincides with the 687 day orbit of Mars about the Sun.

The highlighted analysis period shows that for much of the time that coverage was computed at Deimos, the Sun was above the Deimos southern hemisphere. This shows that sunlit-constrained observations of the southern polar regions were generally more obtainable than those at the northern polar regions.

If the analysis period was shifted to a range of times where the solar latitude was solely at a far northern or far southern point, it is possible that sunlit observations at the opposite pole would not be achievable.

4.4 Deimos DRO Sensitivity

The stability of QSOs, and specifically the critical inclination was previously studied in Section 4.1. To facilitate operations in Mars - Deimos DROs, an understanding of the dynamical sensitivity of these DROs is also required.

While it is very likely that an actual science orbit about Deimos would utilize a QSO rather than a DRO, the stability properties of DROs are favorable for a "walk-in" strategy or as a stable hold point for operations.

Given this, a similar study to the study performed in Section 4.1 was performed to test out the resilience of DROs at Deimos to velocity errors.

The first test case applied velocity errors in the Y direction $\dot{Y}_0$ ranging from -50 to 50 cm/s. For all cases, this perturbation was applied at the X-axis crossing and the spacecraft was propagated for 14 days in the ephemeris force model. Separating out which orbits remained at Deimos with no additional maneuvers and which ones either impacted or left the vicinity of the body, a sensitivity map is shown in Figure 4.19.

This sensitivity map immediately shows the amount of $\dot{Y}_0$ error that is tolerable across members of the f family. This information could drive requirements for actual mission operations such as navigation requirements and maneuver execution error requirements. The requirements themselves would likely be more strict than the values seen here in order to add margin, but these values could be considered the worst-case navigation performance that could still be tolerated without experiencing a potentially mission-ending event.

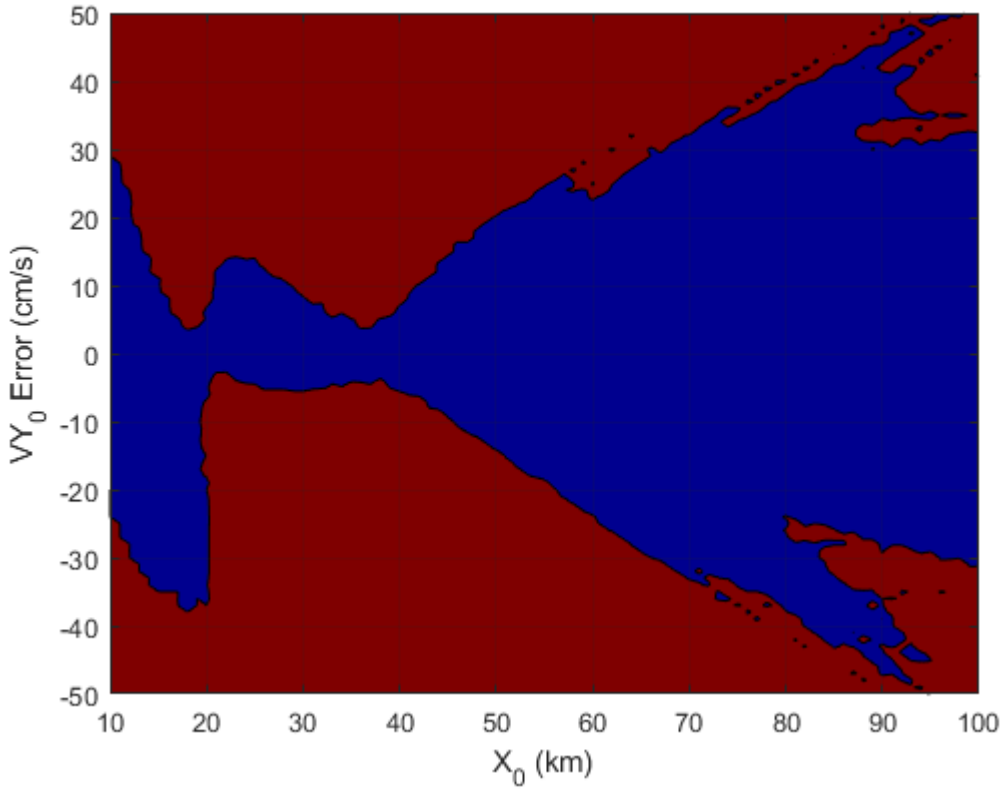

Figure 4.19. $\dot{Y_0}$ sensitivities. Blue: Remains in orbit about Deimos. Red: Impacts or leaves the vicinity of Deimos.

For the $\dot{Y_0}$ sensitivity, there are two regions of the orbital tradespace where a very tight tolerance is required: around $X_0 = 20$ km and $X_0 = 35$ km. Past an X_0 value of 40 km, the sensitivity decreases, eventually allowing $\dot{Y_0}$ errors of up to 30 cm/s.

For designing a mission to Deimos, this information could be used not only to set mission requirements, but also to design CONOPS for transitioning into the final science orbit. For example, if the desired science orbit was at an X_0 value of approximately 35 km, this falls into an extremely sensitive part of the tradespace where any small errors in the injection burn could put the spacecraft on a collision course with Deimos. In order to mitigate risk, it could be a more safe option to inject into a higher altitude DRO where errors in the injection velocity are more tolerable, and

then slowly decrease that altitude using small burns that are unlikely to cause high enough errors to place the spacecraft onto a dangerous trajectory.

A similar study was performed to examine the effect of errors in the X velocity $\dot{X}_0$. Remember that in the CRTBP, the velocity $\dot{X}_0$ should be equal to zero in order to ensure a perpendicular axis crossing. In the ephemeris model, this is not always *exactly* true, but it should be very close to zero.

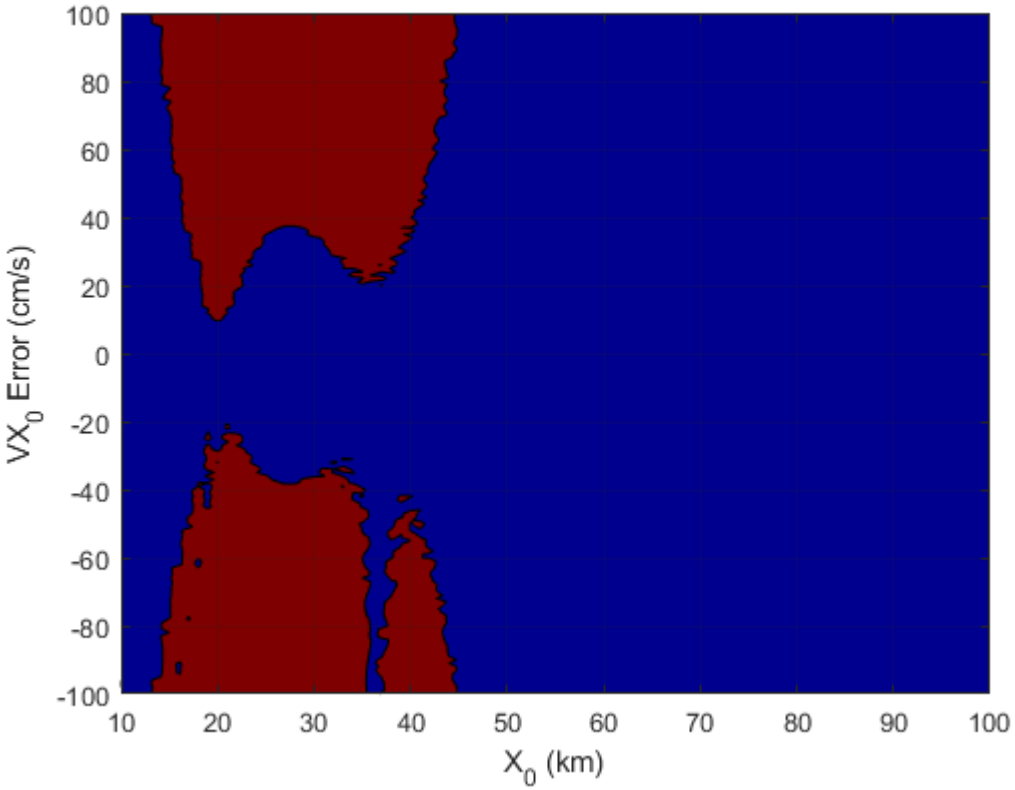

Figure 4.20. $\dot{X}_0$ sensitivities. Blue: Remains in orbit about Deimos. Red: Impacts or leaves the vicinity of Deimos.

Figure 4.20 shows the results for the sensitivities in $\dot{X}_0$. There are some similarities with the $\dot{Y}_0$ sensitivities, but also some key differences. The most sensitive region is still around $X_0 = 20$ km, but once the f family grows past $X_0 = 40$ the allowable error in $\dot{X}_0$ drastically increases. An extended version of this figure is shown in Figure 4.21 that examines $\dot{X}_0$ errors of up to 5 m/s.

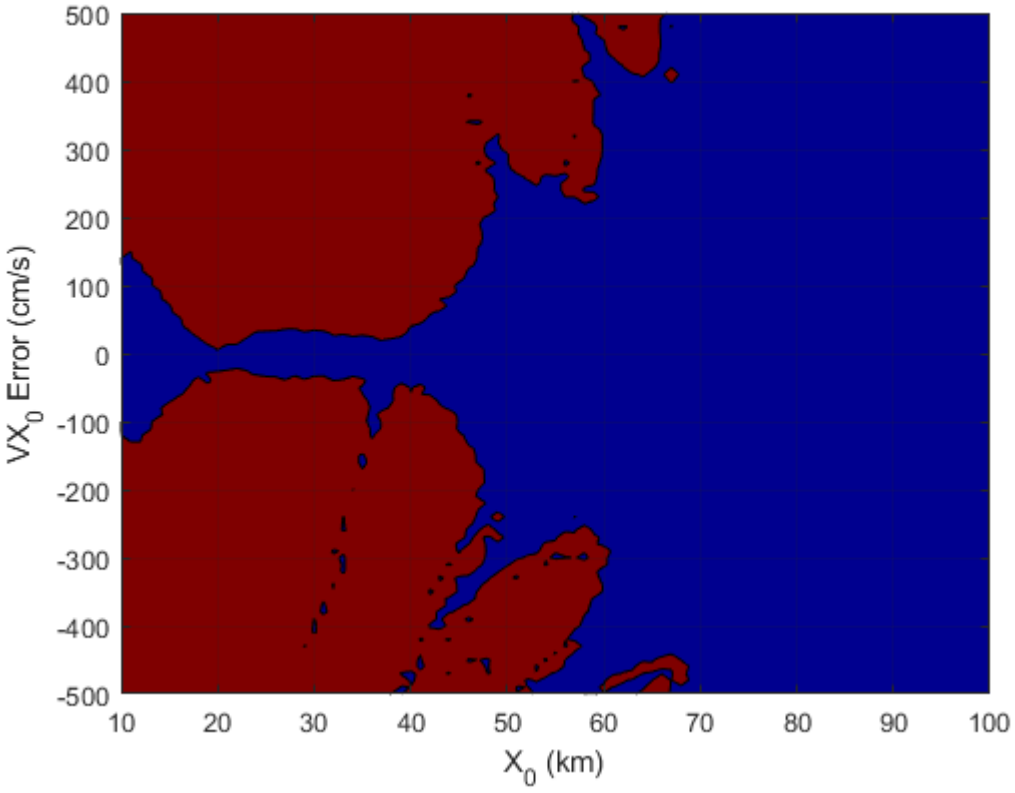

Figure 4.21. $\dot{X}_0$ sensitivities. Blue: Remains in orbit about Deimos. Red: Impacts or leaves the vicinity of Deimos.

This analysis shows that for members of the family outside $X_0 = 50$ km, velocity errors in $\dot{X}_0$ of over 1 m/s can be tolerated without leaving Deimos or impacting the body. This tolerable error is much larger than the error that can be tolerated in $\dot{Y}_0$ for the same members of the family.

An example of an operational benefit from this information could be deciding where in the Deimos orbit about Mars to perform a maneuver or an initial injection into the DRO about Deimos. For ground-based navigation, both range and range-rate measurements only provide information along the Earth - spacecraft line of sight vector. This means that the instantaneous covariance in the direction of this vector is usually much smaller than the covariance perpendicular to the vector.

Given that there is one direction where the navigational knowledge is much better than every other direction, it would make sense to align this direction with the direction that is most sensitive to navigation or other errors if the mission has the flexibility to do so.

4.5 Transfers Between Orbits

How to perform transfers between QSOs is still an ongoing subject of research in the literature particularly driven by the *MMX* mission [17]. For this thesis, a preliminary study on the fuel requirements for transfers between planar DROs (members of the f family) at Deimos was performed.

4.5.1 Along-Track Three-Burn Strategy

The first strategy examined was a three burn strategy in the Deimos along-track direction. These are three burns performed at X-axis crossings that only change the velocity in the Y direction $\dot{Y}$. This strategy is valid for both increasing and decreasing orbital altitude.

For testing these transfers in the ephemeris model, a grid of transfers was designed between a set of DROs parameterized by their X_0 values. This shows the fuel cost in terms of delta-v for a transfer between any two members of the Deimos f family with values of X_0 between 10 and 100 km. The results are shown in Figure 4.23, and show that it is possible to transverse between any two members of the analyzed portion of the family via this method for transfers on the order of 0-3 m/s.

4.5.2 Radial Three-Burn Strategy

One potential downside to the first analyzed transfer method is its lack of resilience to missed-thrust events. As shown in Section 4.4, errors in $\dot{Y}$ applied at X-axis crossings can put a spacecraft onto a trajectory that will impact Deimos or escape

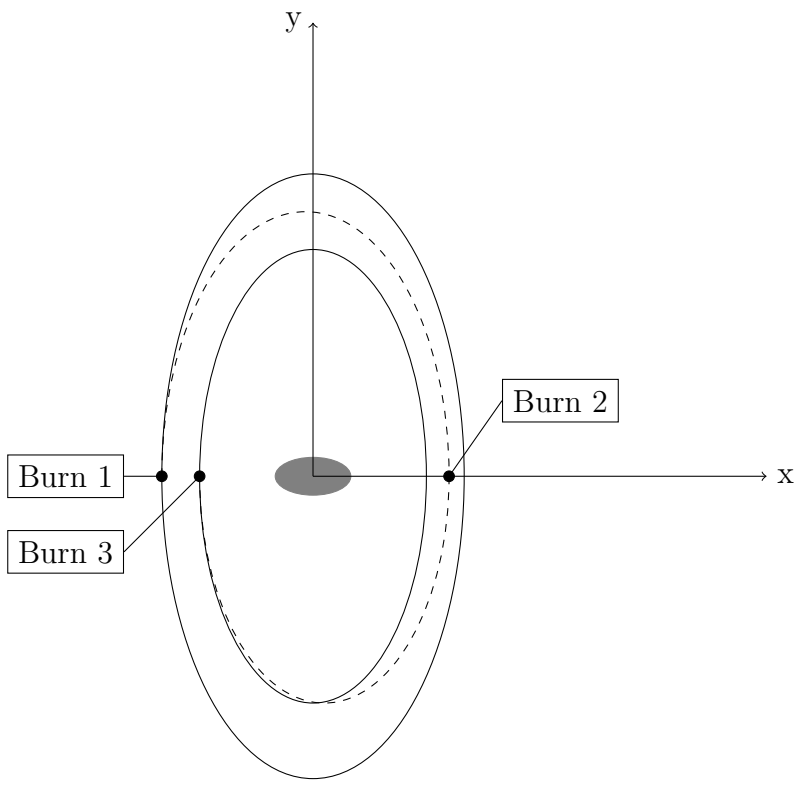

Figure 4.22. Three-burn along-track strategy for transfers at Deimos.

the Deimos vicinity if no additional corrections are performed. The first burn in the previous three-burn strategy will often place the spacecraft onto a potentially dangerous trajectory if the second or third burn is missed.

To attempt to mitigate these potentially dangerous transfers, an alternative strategy is proposed that performs three burns in the radial direction *with respect to Mars*. That radial direction is aligned with the X-axis in the coordinate frame that we have utilized. This strategy is shown in Figure 4.24.

Much like the previous strategy, this strategy works for increasing or decreasing altitude with respect to Deimos. However, it comes with an increased delta-v cost when compared to the previous method. The corresponding delta-v grid for this method of transfers among the f family is shown in Figure 4.25.

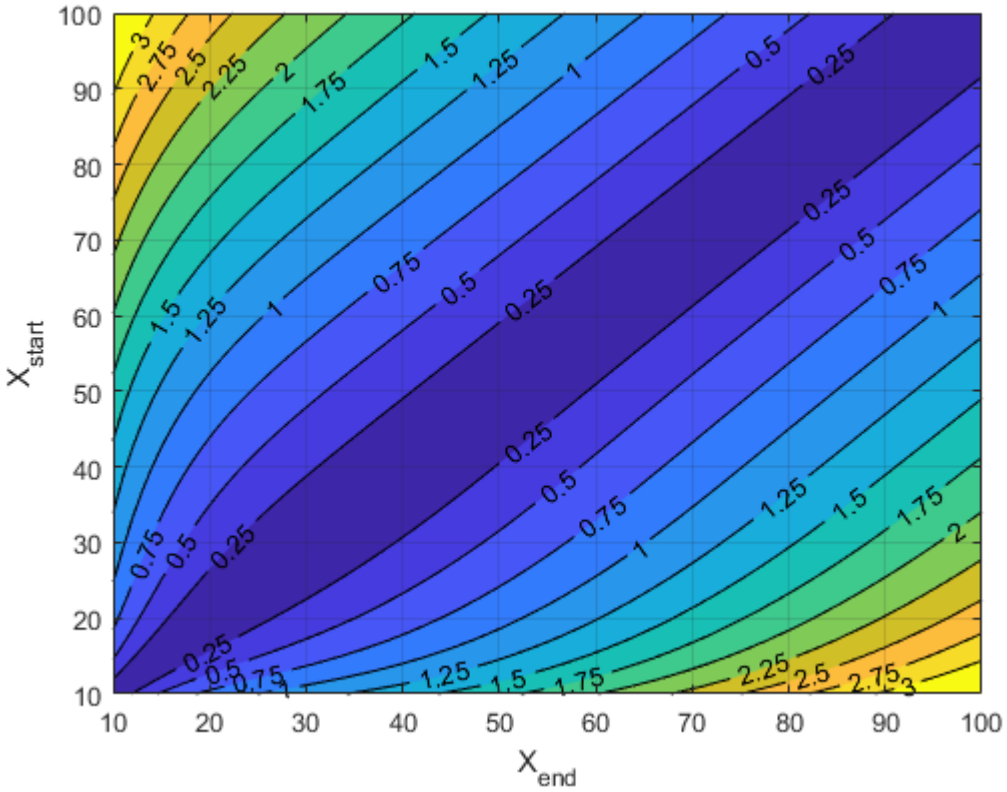

Figure 4.23. A map of transfers between members of the f family via the Along-Track Three-Burn Strategy in m/s.

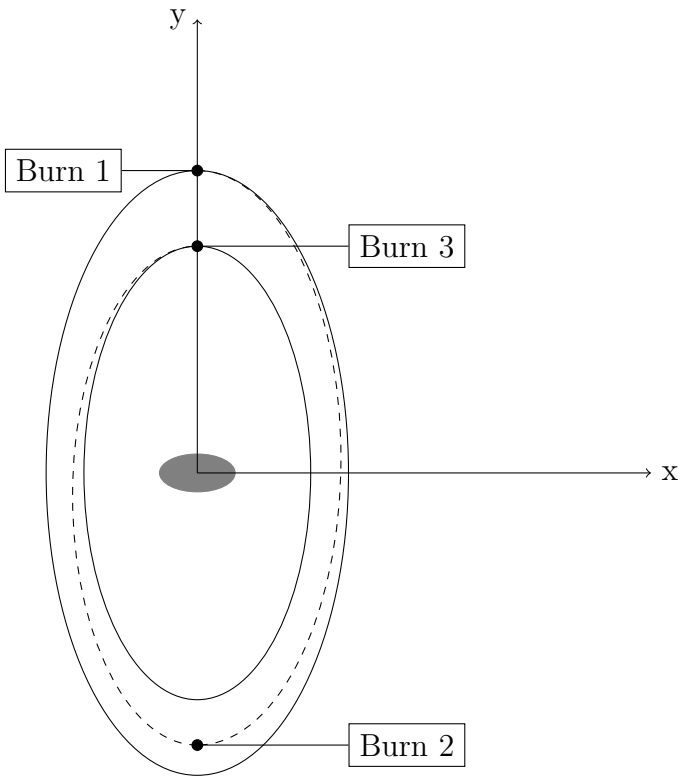

Figure 4.24. Three-burn radial strategy for transfers at Deimos.

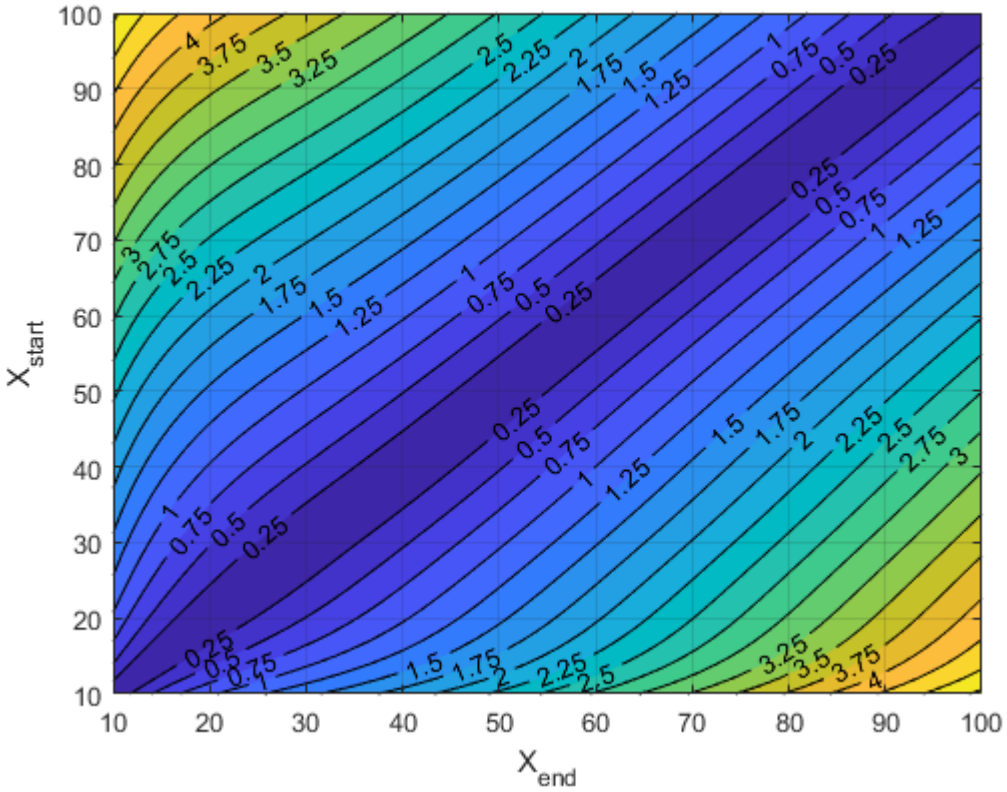

Figure 4.25. A map of transfers between members of the f family via the Radial Three-Burn Strategy in m/s.

5. CONCLUSIONS AND FUTURE WORK

This thesis has examined the dynamical environment of trajectories in the Mars - Deimos system and provided a science orbit design using a set of notional instruments for a remote sensing mission to the moon. In addition to this, sensitivity analyses were performed to inform future navigation requirements at the body. Finally, strategies for performing transfers between planar DROs at Deimos were studied and simulated. The goal of this work was ultimately to inform current and future mission concepts to the Deimos system.

Close-proximity trajectories to Deimos are best studied in the context of the Mars - Deimos three-body problem. In this dynamical model, there mathematically exists a small set of prograde orbits about Deimos, but many of these trajectories intersect the Deimos surface or are too unstable to be utilized in an operational setting. Distant retrograde orbits about Deimos provide very promising stability characteristics for a mission dedicated to the body. Quasi-satellite orbits can be generated by adding out of plane velocities to distant retrograde orbits. These trajectories maintain some of the stability properties of DROs, but have more favorable viewing geometry for performing remote sensing observations, particularly of polar regions.

The stability properties of these QSOs were examined to determine how much out of plane motion was possible before the trajectories were destabilized by Martian perturbations. Additional sensitivity analyses were performed in order to study the effect of velocity errors in Deimos DROs, which will inform navigation requirements and future CONOPS for the timing of maneuvers during a "walk-in" strategy.

Modeling a notional suite of remote sensing instruments and a realistic set of science requirements, a batch search method was performed in order to find potential science orbits that maximize the surface coverage of Deimos at the desired spatial resolutions. With the analyzed set of requirements and instruments, a number of

QSOs with a closest approach to Deimos of 40-50 km and a relative inclination of around 140 degrees maximize global coverage of the body. For observations in the visual band, a near-global map with multiple solar geometries at 5 m/px is possible, and a similar map is possible in the thermal infrared band at 10 m/px.

The exact performance values that are possible are, of course, a function of the actual instruments used on a spacecraft, the CONOPS for gathering the data, and a large number of other mission-specific factors. However, this analysis has shown that with a set of ambitious remote sensing science requirements and a set of realistic instruments, obtaining near-global coverage is possible using QSOs about Deimos. These trajectories provide a very promising opportunity for the scientific exploration of Deimos and could pave the way towards answering questions about the origins of both Martian moons and pathfinding for future human exploration of Mars.

5.1 Recommendations for Future Work

This future work section will focus on some of the key mission design and navigation steps that would be required in order to develop a mature mission concept to Deimos utilizing QSOs.

Dynamical Model Uncertainties

In Section 3.2, the current uncertainties on the Deimos GM value were discussed. The impact of these uncertainties on the location of Lagrange points was demonstrated, but the resulting impact on initial conditions for DROs and QSOs was not examined. An understanding of the possible range of initial conditions for these orbits based on uncertainties in the Deimos GM value will be required for any mission that eventually does want to utilize a close-proximity orbit to Deimos.

Additionally, as discussed in Section 2.5, the ephemeris propagations in this analysis are performed with a Deimos spherical harmonic model, but only a point mass model for Mars. Inside approximately 25 km, the spherical harmonic model for

Deimos is likely more significant than that of Mars, but performing the stability analyses shown in this thesis using spherical harmonic models for both bodies could possibly provide additional insights into operations at Deimos.

Navigation Studies

It was previously speculated that a period of co-estimation of the Deimos GM value during navigation would likely be required before any close-proximity trajectories would be possible. Further work simulating how far the covariance on this parameter can be decreased and the period of time required to do so would be immensely useful. For the *MMX* mission, refining the Phobos gravity model from a higher orbit is a part of the operational workflow, so in the coming years, there will likely be published literature on this topic for Phobos. These studies will hopefully be of use towards performing a similar strategy at Deimos.

In conjunction with these navigation studies, it could be interesting to experiment with methods of onboard optical navigation in the vicinity of Deimos. Optical navigation has the potential to ease the burden on a consistently over-subscribed Deep Space Network and assist in providing some level of spacecraft autonomy during operations.

Operational Stationkeeping Strategies

In order to generate QSOs for use in the long-term coverage analyses in Section 4.2.2, the addition of stationkeeping maneuvers was required. The method for designing these maneuvers was described in this thesis, but to summarize, it targeted maneuvers during every relative orbit about Deimos. While effective in maintaining long-term QSOs for use in analysis, this stationkeeping strategy is likely operationally unfeasible. The total delta-v required is small, but a cadence of one or more maneuvers per day would be extremely challenging from an operations perspective. Future work should be dedicated towards designing stationkeeping strategies such that ma-

neuvers are required at no more than once every few days. This is a maneuver cadence that is more realistic for a future mission.

Eclipsing Conditions

Given that spacecraft in DROs are in a constant plane with respect to their primary body (Mars in this case), they are particularly susceptible to seasonal eclipses when that plane aligns with the Sun - Mars vector. QSOs are similarly susceptible. For the ideal science orbit shown in Figure 4.16 propagated out over an entire Martian year, there are two sets of three-month periods out of each Martian year where Mars eclipses occur with each orbit of Deimos about Mars. These Mars eclipses last up to 1.5 hours each. Dynamically, there is very little that can be done about these eclipses, as the entire vicinity around Deimos is eclipsed.

There are also Deimos eclipses that occur around the same time in the Martian year, but can be significantly longer. Most are on the order of 1-2 hours, but for the trajectory shown in Figure 4.16 propagated for an entire Martian year, there are Deimos eclipses of up to 9 hours long. The survivability of these long eclipses could be much more challenging for a spacecraft than the shorter Mars eclipses, but could also be avoided via an orbital maneuver or precise phasing in a QSO.

Canalias et al. have studied strategies for minimizing the length of Phobos eclipses in QSOs by utilizing synodic resonance in support of the *MMX* mission design [19]. A similar approach could be taken for trajectories about Deimos in order to design Deimos QSOs that could be used operationally.

REFERENCES

[1] David A. Minton, Briony H. N. Horgan, David A. Spencer, Mayank Aggarwal, Rohan Deshmukh, Jacob R. Elliot, Andrew J. Hesselbrock, Connor R. Tinker, Zachary R. Putnam, Giusy Falcone, Destiny M. Fawley, Elizabeth M. Fleming, Thomas R. Smith, James W. Williams, Philip R. Christensen, Erik Asphaug, Jordi Puig-Suari, Austin Williams, Matija Cuk, Francesca DeMeo, Masatoshi Hirabayashi, Jean-Francois Smekens, and Andrew Rivkin. Chariot: A small satellite concept mission to explore the enigmatic moons of Mars. Technical report, Purdue University, 2018.

[2] Scott L. Murchie, Daniel T. Britt, and Carle M. Pieters. The value of Phobos sample return. *Planetary and Space Science*, 102(C):176–182, 2014.

[3] Scott L. Murchie, Nick Thomas, Daniel T. Britt, Ken Herkenhoff, and James F. Bell. Mars Pathfinder spectral measurements of Phobos and Deimos: Comparison with previous data. *Journal of Geophysical Research E: Planets*, 104(E4):9069–9079, 1999.

[4] A. S. Rivkin, R. H. Brown, D. E. Trilling, J. F. Bell, and J. H. Plassmann. Near-infrared spectrophotometry of Phobos and Deimos. *Icarus*, 156(1):64–75, 2002.

[5] Carle M. Pieters, Scott Murchie, Nicolas Thomas, and Daniel Britt. Composition of surface materials on the moons of Mars. *Planetary and Space Science*, 102(C):144–151, 2014.

[6] Michael W. Busch, Steven J. Ostro, Lance A.M. Benner, Jon D. Giorgini, Christopher Magri, Ellen S. Howell, Michael C. Nolan, Alice A. Hine, Donald B. Campbell, Irwin I. Shapiro, and John F. Chandler. Arecibo radar observations of Phobos and Deimos. *Icarus*, 186(2):581–584, 2007.

[7] Ariel N. Deutsch, James W. Head, Kenneth R. Ramsley, Carle M. Pieters, Ross W.K. Potter, Ashley M. Palumbo, Michael S. Bramble, James P. Cassanelli, Erica R. Jawin, Lauren M. Jozwiak, Hannah H. Kaplan, Connor F. Lynch, Alyssa C. Pascuzzo, Le Qiao, and David K. Weiss. Science exploration architecture for Phobos and Deimos: The role of Phobos and Deimos in the future exploration of Mars. *Advances in Space Research*, 62(8):2174–2186, 2018.

[8] R. Z. Sagdeev and A. V. Zakharov. Brief history of the Phobos mission. *Nature*, 341(6243):581–585, 1989.

[9] R. Z. Sagdeev and A. V. Zakharov. A brief history of the expedition to Phobos. *Soviet Astronomy Letters*, 16, 1990.

[10] M. Ya Marov, V. S. Avduevsky, E. L. Akim, T. M. Eneev, R. S. Kremnev, S. D. Kulikov, K. M. Pichkhadze, G. A. Popov, and G. N. Rogovsky. Phobos-Grunt: Russian sample return mission. *Advances in Space Research*, 33(12):2276–2280, 2004.

[11] Thomas C. Duxbury, Alexander V. Zakharov, Harald Hoffmann, and Edward A. Guinness. Spacecraft exploration of Phobos and Deimos. *Planetary and Space Science*, 102(C):9–17, 2014.

[12] O. Witasse, T. Duxbury, A. Chicarro, N. Altobelli, T. Andert, A. Aronica, S. Barabash, J. L. Bertaux, J. P. Bibring, A. Cardesin-Moinelo, A. Cichetti, V. Companys, V. Dehant, M. Denis, V. Formisano, Y. Futaana, M. Giuranna, B. Gondet, D. Heather, H. Hoffmann, M. Holmström, N. Manaud, P. Martin, K. D. Matz, F. Montmessin, T. Morley, M. Mueller, G. Neukum, J. Oberst, R. Orosei, M. Pätzold, G. Picardi, R. Pischel, J. J. Plaut, A. Reberac, P. Pardo Voss, T. Roatsch, P. Rosenblatt, S. Remus, N. Schmedemann, K. Willner, and T. Zegers. Mars Express investigations of Phobos and Deimos. *Planetary and Space Science*, 102(C):18–34, 2014.

[13] O. Sharaf, S. Amiri, S. Al Meheiri, M. Wali, Z. Al Shamsi, A. Al Rais, I. Al Qasim, K. Al Harmoodi, N. Al Teneiji, H. Almatroushi, Me. Al Shamsi, Ma. Al Shamsi, E. Al Teneiji, A. Al Janaahi, M. McGrath, P. Withnell, N. Ferrington, H. Reed, B. Landin, D. Brain, J. Deighan, M. Chaffin, G. Holsclaw, G. Drake, C. Edwards, M. Wolff, R. Lillis, M. Smith, and F. Forget. Emirates Mars Mission (EMM) Overview. In *19th EGU General Assembly*, 2017.

[14] Stefano Campagnola, Chit Hong Yam, Yuichi Tsuda, Ogawa Naoko, and Yasuhiro Kawakatsu. Mission analysis for the Martian Moons Explorer (MMX) mission. *Acta Astronautica*, 146(March):409–417, 2018.

[15] Jürgen Oberst, Kai Wickhusen, Konrad Willner, Klaus Gwinner, Sofya Spiridonova, Ralph Kahle, Andrew Coates, Alain Herique, Dirk Plettemeier, Marina Díaz-Michelena, Alexander Zakharov, Yoshifumi Futaana, Martin Pätzold, Pascal Rosenblatt, David J. Lawrence, Valery Lainey, Alison Gibbings, and Ingo Gerth. DePhine – The Deimos and Phobos Interior Explorer. *Advances in Space Research*, 62(8):2220–2238, 2018.

[16] Paulo J.S. Gil and Julia Schwartz. Simulations of quasi-satellite orbits around Phobos. *Journal of Guidance, Control, and Dynamics*, 33(3):901–914, 2010.

[17] Hitoshi Ikeda, Shinji Mitani, Yuya Mimasu, Go Ono, Kenichiro Nigo, and Yasuhiro Kwakatsu. Orbital Operations Strategy in the Vicinity of Phobos. *International Symposium on Space Flight Dynamics*, 2017.

[18] E.L. Akim, G.A. Popov, and A.G. Tuchin. Mechanics and Motion Control of a Space Vehicle in the Project of Relict Substance Delivery on Earth (the Project Phobos_Grunt). *IFAC Proceedings Volumes*, 37(6):209–214, 2004.

[19] Elisabet Canalias, Laurence Lorda, Hongru Chen, and Hitoshi Ikeda. Trajectory Design and Operational Challenges for the Exploration of Phobos. In *AAS/AIAA Astrodynamics Specialist Conference*, pages 1–15, 2020.

[20] Elisabet Canalias, Laurence Lorda, Thierry Martin, Julien Laurent-Varin, Jean Charles, and Yuya Mimasu. Trajectory analysis for the Phobos proximity phase of the MMX mission. *Proceedings of 26th International Symposium on Spaceflight Dynamics*, pages 1–9, 2017.

[21] Scott W. Jansson. Stable Orbits About the Martian Moons, 1989.

[22] Frank Luria. Analysis of Periodic Orbits About the Martian Moons by Continuation Techniques, 1990.

[23] William E. Wiesel. Stable orbits about the Martian moons. *Journal of Guidance, Control, and Dynamics*, 16(3):434–440, 1993.

[24] J. Rahe, L. Mukhin, R. Sagdeev, K. Karavasilis, J. Trombka, A. Zakharov, A. Medvedev, V. Khatulev, and V. Yuriev. Low cost mission to Phobos and Deimos. *Acta Astronautica*, 45(4-9):301–309, 1999.

[25] Yanping Guo. Deimos rendezvous orbit design for the MERLIN mission. In *AIAA/AAS Astrodynamics Specialist Conference 2012*, 2012.

[26] Daniel J. Scheeres. *Orbital Motion in Strongly Perturbed Environments*. Springer-Praxis Books in Astronautical Engineering, 2012.

[27] Sofya Spiridonova, Kai Wickhusen, Ralph Kahle, and Jurgen Oberst. Quasi-Satellite Orbits around Deimos and Phobos motivated by the DePhine Mission Proposal. *Proceedings of 26th International Symposium on Spaceflight Dynamics*, 2017.

[28] Nicola Baresi, Lamberto Dell'Elce, Josué Cardoso dos Santos, and Yasuhiro Kawakatsu. Long-term evolution of mid-altitude quasi-satellite orbits. *Nonlinear Dynamics*, 99(4):2743–2763, 2020.

[29] K. Nishimura, S. Satoh, and K. Yamada. Analysis of a distant retrograde orbit in the Hill three-body problem. *Acta Astronautica*, 170(April 2019):365–374, 2020.

[30] Amanda F. Haapala. *Trajectory Design in the Spatial Circular Restricted Three-Body Problem Exploiting Higher-Dimensional Poincaré Maps*. PhD thesis, Purdue University, 2014.

[31] V. Szebehely. Application of the restricted problem of three bodies to space mechanics. *Space Science Reviews*, 2(2):219–249, 1963.

[32] H. Poincaré. *Les Méthodes Nouvelles de la Mécanique Céleste, Tome 1. Solutions Périodiques; Non-Existence des Intégrales Uniformes. Solutions Asymptotiques*. Paris, 1892.

[33] Alain Chenciner. Poincaré and the Three-Body Problem. In *Progress in Mathematical Physics*, volume 83, pages 51–149. Birkhäuser, Boston, 2015.

[34] M. Hénon and Monique Guyot. Stability of Periodic Orbits in the Restricted Problem. In *Periodic Orbits, Stability and Resonances*, pages 349–374, 1970.

[35] M. Hénon. Exploration numérique du problème restreint. II. Masses égales, stabilité des orbites périodiques. *Annales d'Astrophysique*, 28, 1965.

[36] M. Hénon. Numerical Exploration of the Restricted Problem. V. Hill's Case: Periodic Orbits and Their Stability. *Astronomy and Astrophysics*, pages 223–238, 1969.

[37] A.E. Roy and M.W. Ovenden. On the Occurance of Commensurable mean motions in the Solar System II. The Mirror Theorem. *Monthly Notices of the Royal Astronomical Society*, 1955.

[38] M. Hénon. *Generating Families in the Restricted Three-Body Problem*. Springer-Verlag, Berlin, 1997.

[39] Steven P. Hughes, Rizwan H. Qureshi, D. Steven Cooley, Joel J. K. Parker, and Thomas G. Grubb. Verification and Validation of the General Mission Analysis Tool (GMAT). In *AIAA/AAS Astrodynamics Specialist Conference 2014*, 2014.

[40] William M Folkner, J. G. Williams, Dale H Boggs, Ryan S Park, and Petr Kuchynka. The Planetary and Lunar Ephemerides DE430 and DE431. *Interplanetary Network Progress Report*, 42(196), 2014.

[41] Robert Jacobson. Revised Ephemerides of the Martian Satellites. In *AAS Division of Dynamical Astronomy Meeting*, 2012.

[42] David Parry Rubincam, Benjamin Fong Chao, and Peter C. Thomas. The gravitational field of Deimos. *Icarus*, 114(1):63–67, 1995.

[43] B. A. Archinal, C. H. Acton, M. F. A'Hearn, A. Conrad, G. J. Consolmagno, T. Duxbury, D. Hestroffer, J. L. Hilton, R. L. Kirk, S. A. Klioner, D. McCarthy, K. Meech, J. Oberst, J. Ping, P. K. Seidelmann, D. J. Tholen, P. C. Thomas, and I. P. Williams. Report of the IAU Working Group on Cartographic Coordinates and Rotational Elements: 2015. *Celestial Mechanics and Dynamical Astronomy*, 130(3):1–46, 2018.

[44] Douglas P. Hamilton and Alexander V. Krivov. Dynamics of distant moons of asteroids. *Icarus*, 128(1):241–249, 1997.

[45] P. C. Thomas, B. Carcich, J. Veverka, C. P. Yoder, S. P. Synnott, H. Salo, J. F. Bell III, R. P. Binzel, G. J. Black, B. E. Clark, M. J. Gaffey, P. Helfenstein, P. D. Nicholson, D. Simonelli, and B. H. Zellner. Small Body Optical Shape Models, 2000.

[46] C. M. Ernst, O. S. Barnouin, and R. T. Daly. The Small Body Mapping Tool (SBMT) for Accessing, Visualizing, and Analyzing Spacecraft Data in Three Dimensions. In *49th Lunar and Planetary Science Conference*, volume 2018, pages 12–13, 2018.

[47] Alex S Konopliv, Charles F Yoder, E Myles Standish, Dah-ning Yuan, and William L Sjogren. A global solution for the Mars static and seasonal gravity , Mars orientation, Phobos and Deimos masses, and Mars ephemeris. *Icarus*, 182:23–50, 2006.

[48] D. Benest. Effects of the Mass Ratio on the Existence of Retrograde Satelllites in the Circular Plane Restricted Problem. *Astronomy and Astrophysics*, 32:39–46, 1974.

[49] Collin Bezrouk and Jeffrey Parker. Long duration stability of distant retrograde orbits. In *AIAA/AAS Astrodynamics Specialist Conference 2014*, 2014.

[50] W. H. Clohessy and R. S. Wiltshire. Terminal Guidance System for Satellite Rendezvous. *Journal of the Aerospace Sciences*, 27(9):653–658, 1960.

[51] Thomas A. Lovell and David A. Spencer. Relative orbital elements formulation based upon the Clohessy-Wiltshire equations. *Journal of the Astronautical Sciences*, 61(4):341–366, 2014.

[52] Mikhail L'vovich Lidov and M.A. Vashkov'yak. On Quasi-Satellite Orbits in a Restricted Elliptic Three-Body Problem. *Pis'ma v Astronomicheskii Zhurnal*, 20:781 – 795, 1994.

[53] S. Mikkola, K. Innanen, P. Wiegert, M. Connors, and R. Brasser. Stability limits for the quasi-satellite orbit. *Monthly Notices of the Royal Astronomical Society*, 369(1):15–24, 2006.

[54] C. de la Fuente Marcos and R. de la Fuente Marcos. Asteroid (469219) 2016 HO3, the smallest and closest Earth quasi-satellite. *Monthly Notices of the Royal Astronomical Society*, 462(4):3441–3456, 2016.

[55] Alexandre Pousse, Philippe Robutel, and Alain Vienne. On the co-orbital motion in the planar restricted three-body problem: the quasi-satellite motion revisited. *Celestial Mechanics and Dynamical Astronomy*, 128(4):383–407, 2017.

[56] Vladislav V. Sidorenko, Anatoly I. Neishtadt, Anton V. Artemyev, and Lev M. Zelenyi. Quasi-satellite orbits in the general context of dynamics in the 1:1 mean motion resonance: perturbative treatment. *Celestial Mechanics and Dynamical Astronomy*, 120(2):131–162, 2014.

[57] M. Hénon. Vertical Stability of Periodic Orbits in the Restricted Problem: II. Hill's Case. *Astronomy and Astrophysics*, 30:317–321, 1974.

[58] Martin Lara, Ryan Russell, and Benjamin Villac. Classification of the distant stability regions at Europa. *Journal of Guidance, Control, and Dynamics*, 30(2):409–418, 2007.

[59] Francisco da Silva Pais Cabral. On the Stability of Quasi-Satellite Orbits in the Elliptic Restricted Three-Body Problem Application to the Mars-Phobos System, 2011.

[60] Collin Bezrouk and Jeffrey S. Parker. Long term evolution of distant retrograde orbits in the Earth-Moon system. *Astrophysics and Space Science*, 362(9), 2017.

VITA

Michael Thompson is a M.S. student at Purdue University in the Space Flight Projects Laboratory. His major and minor concentrations are "Astrodynamics and Space Applications" and "Computational Science and Engineering" respectively. In addition to his academic work, he works as an Astrodynamics Engineer at Advanced Space, a company providing mission design, navigation, and other spacecraft services in Boulder, CO.

Education

M.S. Aeronautics and Astronautics, Purdue University, December 2020. Thesis title: "Design of Quasi-Satellite Science Orbits at Deimos."

B.S. Aeronautical and Astronautical Engineering, Purdue University, December 2017.

Conference Publications

Michael R. Thompson, Mitchell W. Dominguez, and David A. Spencer. Science Orbit Design for a Deimos Mission. *AIAA/AAS Astrodynamics Specialist Conference*, 2020.

Nathan L. Parrish, Matthew J. Bolliger, Ethan Kayser, Michael R. Thompson, Jeffrey S. Parker, Bradley W. Cheetham, Diane C. Davis, and Daniel J. Sweeny. Near Rectilinear Halo Orbit Determination with Simulated DSN Observations. *AIAA SciTech 2020 Forum*, 2020.

Nathan L. Parrish, Ethan Kayser, Matthew J. Bolliger, Michael R. Thompson, Jeffrey S. Parker, Bradley W. Cheetham, Diane C. Davis, and Daniel J. Sweeny. Ballistic Lunar Transfers to Near Rectilinear Halo Orbit: Operational Considerations. *AIAA SciTech 2020 Forum*, 2020.

White Papers

Matthew Bolliger, Michael R. Thompson, Nathan P. Ré, and Diane C. Davis. Analysis of Ground-Based Navigation Configurations for Uncrewed Gateway Operations in the 9:2 Near Rectilinear Halo Orbit. 2020.